

Uncertainty in hydrogeophysics: electrical resistivity tomography with variational inference

Jiahe Yan^{1,2}, Zhaofa Zeng², Chak-Hau Michael Tso³, Qinbo Cheng⁴ and Andrew Binley¹

¹Lancaster Environment Centre, Lancaster University, Lancaster LA1 4YQ, UK. E-mail: a.binley@lancaster.ac.uk

²College of Geo-Exploration Science and Technology, Jilin University, Changchun 130026, China

³Digital Research Group, UK Centre for Ecology & Hydrology, Lancaster LA1 4AP, UK

⁴College of Hydrology and Water Resources, Hohai University, Nanjing 210098, China

Accepted 2026 April 7. Received 2026 April 3; in original form 2025 October 21

SUMMARY

Electrical resistivity tomography (ERT) is a widely used and effective tool for hydrogeological investigations. Conventional ERT inversion approaches are based on gradient-based algorithms, which typically provide deterministic optimal solutions, which are subject to uncertainty. Such uncertainty could have significant impact on hydrogeological interpretation using ERT. Model appraisal is a critical step after inversion, however, conventional appraisal methods are qualitative and thus subjective. To address these limitations, this study introduces a probabilistic variational inference method, referred to as Stein variational gradient descent (SVGD), to quantify both resistivity distributions and associated uncertainties in ERT inversions. Synthetic examples are conducted to investigate the effects of configurations and noise, and to compare the performance of SVGD with conventional inversion and model appraisal techniques. A field case study and its model validation are also presented to demonstrate the practical advantages of uncertainty quantification in field. The results indicate that SVGD can effectively reduce artifacts introduced by regularization and provide more comprehensive quantitative insights into subsurface structures compared to conventional approaches. The study also reveals limitations in the interpretation of basic statistics of uncertainty estimates, highlighting the need to examine the entire posterior distributions of parameter values. Additionally, this study demonstrates that the final uncertainty arises from a trade-off among multiple factors, such as geometry of subsurface structures, measurement techniques and data noise levels. Finally, we also discuss some comparisons with other probabilistic frameworks in hydrogeophysics, highlighting its potential to improve uncertainty and probability quantification in ERT and possible future developments in hydrogeophysical coupled inversion.

Key words: Electrical resistivity tomography (ERT); Bayesian inference; Probability distributions; Hydrogeophysics; Hydrology.

1 INTRODUCTION

Geophysical methods are widely used to quantify hydrogeological structures, properties and states (S.S. Hubbard & Y. Rubin 2000; M. Van Camp *et al.* 2006; A. Binley *et al.* 2015; T.C. Johnson *et al.* 2021; M.W. Lubczynski *et al.* 2024; A. Thomas *et al.* 2024). The rapid growth of the field of hydrogeophysics over the past few decades has no doubt been driven by the limited value of traditional investigative methods in characterizing heterogeneous subsurface systems (A. Binley *et al.* 2015). In comparison to traditional borehole-based investigations, geophysical techniques can also be advantageous due to cost and efficiency. However, geophysical methods do not provide direct estimates of properties or states of interest and any quantification is the subject to several sources of uncertainty.

Electrical methods (direct current resistivity and induced polarization) are, arguably, the most popular methods in hydrogeophysics given that they can be sensitive to various properties (e.g. porosity, permeability, etc.), states (e.g. water content, pore fluid salinity, etc.) and more qualitative characteristics, for example, related to texture or fracture density (J. Irving & K. Singha 2010; A. Miltenberger *et al.* 2021; D.A. Ciraula *et al.* 2023; H. Chen *et al.* 2025). In particular, 2-D and 3-D electrical resistivity tomography (ERT) surveys are now routinely used in hydrogeological investigations (e.g. A. Binley *et al.* 2002; A. Kemna *et al.* 2002; G. Cassiani *et al.* 2009; S. Uhlemann *et al.* 2017; N. Claes *et al.* 2020; M.S. Pleasants *et al.* 2022; J.P. Boyd *et al.* 2024a). Many such studies take advantage of the time-lapse capability of the method.

The ERT method typically consists of measuring a set of transfer resistances (or apparent resistivities) based on a large number of four electrode configurations (e.g. A. Binley & L. Slater 2020). These data are then interpreted through an inversion approach in order

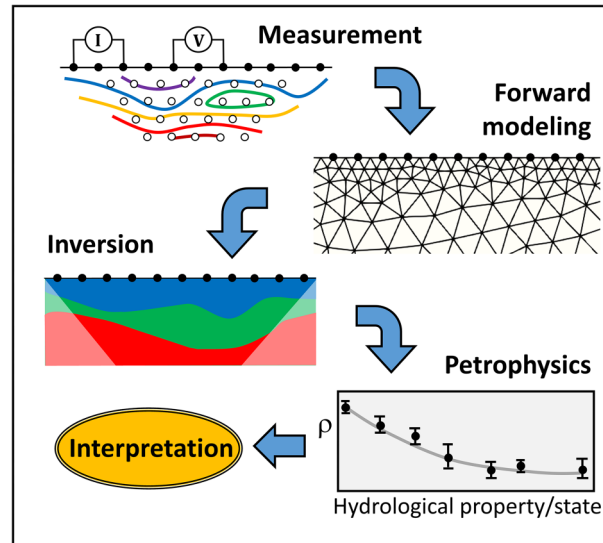


Figure 1. Schematic showing the range of sources of uncertainty in hydrogeophysical applications of ERT.

to produce a model (or models) of subsurface resistivity distribution that is (or are) consistent with the measurements. In the majority of cases, a final single model is derived that represents the best estimate of the subsurface geoelectrical structure. The most common approaches to solving ERT inversion problems are generally gradient-based. Methods such as Gauss–Newton (T. Günther *et al.* 2006; A. Pidlisecky *et al.* 2007), conjugate gradient (B. Liu *et al.* 2012) and Broyden–Fletcher–Goldfarb–Shanno methods (A.L. Codd & L. Gross 2018) convert ERT imaging into optimization problems, which provide deterministic optimal solutions in an iterative manner.

The use of inverse (or optimization) methods to tackle the ERT problem introduces a source of uncertainty—there may be multiple models that match the data to a reasonable degree, which involves the non-uniqueness and equivalence of inverse problems. As fundamental issues of inverse problems, such uncertainty arises from the limited geophysical observations and is definitely unavoidable (R.C. Aster *et al.* 2018). Other sources of uncertainty exist, for example, due to measurement errors (e.g. C.H.M. Tso *et al.* 2017; A. Li *et al.* 2025), forward modelling (C.H.M. Tso *et al.* 2021) and the petrophysical relationships used to translate geophysical parameters to properties or states of interest (e.g. C.H.M. Tso *et al.* 2019), as summarized in Fig. 1. In this paper, we focus on the estimation of uncertainty in the inversion process. While the broader hydrological community widely accepts that models are subject to uncertainty (e.g. K. Beven & A. Binley 2014), and the inherent non-uniqueness and equivalence of inverse problems are well-recognized in geophysics for decades (A. Tarantola 1987), practical estimation of uncertainty in field explorations is important but are still not routinely addressed and quantified (N. Linde *et al.* 2017).

Despite the common lack of quantitative uncertainty estimation in ERT inversion (and other hydrogeophysical methods), model appraisal methods are occasionally used. The depth of investigation approach of D.W. Oldenburg & Y.G. Li (1999) for 2-D problems, and extension to 3-D by G.A. Oldenborger *et al.* (2007), are relatively simple approaches based on a comparison of two inversions subject to different constraints from a reference model. These methods are reasonably practical but their use and interpretation can be somewhat subjective.

Other methods for model appraisal include the model resolution matrix (W. Menke 2015) and, more qualitatively, sensitivity analysis (e.g. A. Kemna 2000). Both approaches construct an appraisal matrix based on the Jacobian (sensitivity) matrix. Low-diagonal values of the resultant matrix indicate regions of low resolution or low sensitivity. However, such appraisal can be somewhat subjective due to the selection of a threshold value (Z.T. Khabaz *et al.* 2024). The model covariance matrix (D.L. Alumbaugh & G.A. Newman 2000; W. Menke 2015) is another method to access the propagation of data and model errors in the inversion. Nonetheless, in poorly resolved regions, value may infer artificially low uncertainty because of the effect of spatial regularization, which can be misleading (A. Binley & L. Slater 2020).

The key problem with the methods discussed so far is that, although they are computationally tractable, they are inherently subjective and do not provide a quantitative estimate of parameter (resistivity) uncertainty. In contrast, a well-established probabilistic inversion framework, known as Bayesian inversion, provides a means of quantifying uncertainty in geophysical (and other) problems. Based on Bayes' rules, posterior distributions can be estimated using Markov chain Monte Carlo (MCMC) sampling and thereafter used to quantify uncertainty in the unknown models (K. Mosegaard & A. Tarantola 1995; K. Gallagher *et al.* 2009). Considering the interest of uncertainty quantification related to ERT, MCMC methods have already been applied to approximate the posterior distribution of subsurface resistivity (A.L. Ramirez *et al.* 2005). However, studies using MCMC in ERT have also encountered common problems found in other geophysical applications, including extremely expensive computational demands, slow convergence and limited scalability, making it unrealistic in practice (X. Zhang & A. Curtis 2020; Z.T. Khabaz *et al.* 2024; X.B. Zhao & A. Curtis 2024a). To address these limitations, recent work mainly focused on reducing model dimensionality and accelerating convergence, such as transdimensional

inversion with Voronoi cells (E. Galetti & A. Curtis 2018), dimensionality reduction based on hydrological processes (E.K. Oware *et al.* 2019) and multimodal non-parametric resistivity modelling (M. Aleardi *et al.* 2021).

Data assimilation, such as Ensemble Kalman inversion (EKI), is another probabilistic approach used for uncertainty quantification. Based on the assumption of a Gaussian posterior distribution, EKI is an approximate Bayesian method that provides a Jacobian-free approach for approximating posterior distributions (C.H.M. Tso *et al.* 2021, 2024). This feature also makes EKI suitable for coupled hydrogeophysical inversion (M. Camporese *et al.* 2015; X.Y. Kang *et al.* 2021), since it is usually challenging to obtain the Jacobian matrix, especially in time-domain hydrogeological simulations such as those based on Richards' equation (S. Weill *et al.* 2009) or solute transport models (D. Pollock & O.A. Cirpka 2012). In C.H.M. Tso *et al.* (2021), the level-set parametrization is used to handle arbitrarily shaped layers and inclusions, which is a type of model hyperparametrization to achieve a reasonable balance between computational efficiency and uncertainty quantification. Although EKI can provide a reasonable approximation of the posterior distribution with relatively small numbers of samples, the uncertainty estimates are usually biased due to the idealized Gaussian posterior hypothesis and model hyperparametrization approach. Nevertheless, because of its highly flexibility and efficiency, EKI remains a valuable contender for uncertainty quantification in ERT and hydrogeophysics in general.

The immense evolution of machine learning methods offers alternative strategies of uncertainty estimation. Such quantification tends to be integrated with neural networks to enable rapid inference after a one-time training process (X.X. Lan *et al.* 2023; B. Liu *et al.* 2023; F. Rincón *et al.* 2025). However, neural networks are still limited by the high cost of data set preparation and training. To achieve comparable accuracy to MCMC methods, they may require more samples and larger data sets (X. Zhang & A. Curtis 2020). Furthermore, under complex near-surface observation conditions (e.g. irregular topography) or variations in field measurements (e.g. different electrode spacings and configurations), the generalization capability of neural networks remains limited in field applications (F. Rincón *et al.* 2025). At present, machine learning methods may be best suited to specific, more constrained problems, although we recognize that this field or research is rapidly developing.

Variational inference (VI) is an alternative framework for Bayesian inference. Unlike the random sampling used in MCMC methods, VI defines a family of probability distributions and converts Bayesian problems into an optimal approximation to the posterior probability distribution function (pdf; X. Zhang *et al.* 2021). This progress is achieved by minimizing the Kullback–Leibler (KL) divergence (S. Kullback & R.A. Leibler 1951), which allows the variational family to approximate the posterior pdf. In this case, VI approaches are more efficient, have good convergence properties and are easily extended to high dimensionality (X.B. Zhao & A. Curtis 2024a). Automatic differential variational inference (ADVI) is one of the most common VI approaches for efficiently approximating the posterior pdf (A. Kucukelbir *et al.* 2017). It computes the gradient of the evidence lower bound (ELBO, equivalent to minimizing the KL divergence) using automatic differentiation and achieves the VI by optimizing to maximize the ELBO. Similar to EKI, it conducts Bayesian inference based on a Gaussian variational family, which is not suitable for multimodal posteriors (X. Zhang & A. Curtis 2020). Therefore, the uncertainty quantification in ADVI is typically biased. Stein variational gradient descent (SVGD) was proposed to avoid Gaussian assumptions by using a set of sample distributions, referred as to ‘particles’, to approximate the posterior (Q. Liu & D.L. Wang 2016). Because SVGD utilizes ‘particle’ densities to represent the target probability distribution, it is particularly effective in capturing multimodal posteriors. In recent years, VI approaches have exhibited excellent performance with seismic methods (X.B. Zhao & A. Curtis 2024a, b; X. Zhang & A. Curtis 2024b), offering new opportunities for uncertainty quantification in complex geophysical problems with reduced computational demands. However, these methods have not yet been applied to quantify uncertainties in ERT.

In this paper, we examine the effectiveness of the SVGD method for quantifying resistivity distributions and associated uncertainties in hydrogeophysics. We begin by introducing the basic principles of both the conventional Gauss–Newton inversion and the SVGD methods for ERT. Two synthetic examples are used to explore the effects of configurations and data noise. We then demonstrate the method for a field example, using field data from a study watershed and a synthetic model validation to demonstrate the practical advantages of the SVGD method and present its probabilistic interpretation. We then discuss our findings and highlight the method's advantages and limitations, and offer some perspective for future work using the SVGD method. Some additional insights into a probabilistic framework are also discussed for a deeper understanding of the uncertainty quantification in hydrogeophysics.

2 METHODS

2.1 Electrical resistivity tomography

ERT inversion is essentially an optimization problem by partial differential equations. The corresponding forward equation can be expressed as:

$$\mathbf{d}_{\text{fwd}} = \mathbf{F}(\mathbf{m}), \quad (1)$$

where \mathbf{m} denotes the resistivity model. We use the logarithm of resistivity to represent subsurface space. \mathbf{F} is the forward operator and \mathbf{d}_{fwd} represents the forward modelled data. To perform ERT inversion, an object function is most commonly defined as

$$\Phi(\mathbf{m}) = \Phi_{\text{d}}(\mathbf{m}) + \alpha \Phi_{\text{m}}(\mathbf{m}), \quad (2)$$

where

$$\Phi_d(\mathbf{m}) = \|\mathbf{W}_d(\mathbf{d}_{\text{fwd}} - \mathbf{d}_{\text{obs}})\|_2^2, \quad (3)$$

$$\Phi_m(\mathbf{m}) = \|\mathbf{W}_m \mathbf{m}\|_2^2, \quad (4)$$

where $\Phi_d(\mathbf{m})$ is the data misfit, α is a regularization scalar and $\Phi_m(\mathbf{m})$ is the model regularization. $\|\cdot\|_2^2$ denotes the L_2 -norm of the vector. \mathbf{d}_{obs} is the vector of observed data, representing transfer resistance in this study. \mathbf{W}_m is the roughness matrix used to apply smoothness regularization to the resistivity model. \mathbf{W}_d is a diagonal data weighting matrix used to balance the weight of observed data.

Following D.J. LaBrecque *et al.* (1996), \mathbf{W}_d , in this study, is given by:

$$\mathbf{W}_{d,ii} = 1.0/\sqrt{a^2 + b^2 d_{\text{obs},i}^2}, \quad (5)$$

where $d_{\text{obs},i}$ is the i -th value of the observed data \mathbf{d}_{obs} . a and b are the coefficients for the data weight. These two coefficients are obtained by expanding the variance as the first two even terms of a Taylor series about $d_{\text{obs},i}$, which are typically estimated statistically based on analysis of reciprocal errors in field measurements in practice (D.J. LaBrecque *et al.* 1996). Coefficient a corresponds to the constant component of the data variance (e.g. the offset error), while coefficient b corresponds to proportionality errors (C.H.M. Tso *et al.* 2017).

The Gauss–Newton method is used in this study to obtain optimal solutions by minimizing eq. (2). The normal equation at the k -th iteration is defined as (A. Binley & L. Slater 2020)

$$(\mathbf{J}_k^T \mathbf{W}_d^T \mathbf{W}_d \mathbf{J}_k + \alpha_k \mathbf{R}) \Delta \mathbf{m}_k = -\mathbf{J}_k^T \mathbf{W}_d^T \mathbf{W}_d (\mathbf{d}_{\text{fwd},k} - \mathbf{d}_{\text{obs}}) - \alpha_k \mathbf{R} \mathbf{m}_k, \quad (6)$$

where $\mathbf{R} = \mathbf{W}_m^T \mathbf{W}_m$. \mathbf{J}_k is the Jacobian matrix, and α_k is the regularization scale at the k -th iteration. The model update $\Delta \mathbf{m}_k$ is obtained by solving eq. (6). Subsequently, the iteration processes $\mathbf{m}_{k+1} = \mathbf{m}_k + \Delta \mathbf{m}_k$ and continues the optimization until the target root-mean-square (RMS) error is reached or the solution is considered to have converged.

While regularization stabilizes the inversion process and reduces artifacts caused by noise, it inevitably compromises model resolution to some extent. Therefore, model appraisal is essential. A model resolution matrix (MRM) \mathbf{R}_m is defined to evaluate the reliability of the inverted model (D.L. Alumbaugh & G.A. Newman 2000), and is expressed as

$$\mathbf{m}_k = \mathbf{R}_m \mathbf{m}_{\text{true}}, \quad (7)$$

where \mathbf{m}_{true} is the (unknown) true resistivity model. Combining eq. (6), the MRM is given by

$$\mathbf{R}_m = (\mathbf{J}_k^T \mathbf{W}_d^T \mathbf{W}_d \mathbf{J}_k + \alpha_k \mathbf{R})^{-1} \mathbf{J}_k^T \mathbf{W}_d^T \mathbf{W}_d \mathbf{J}_k, \quad (8)$$

where \mathbf{J}_k is the Jacobian matrix calculated using the final inversion result and α_k denotes the final regularization scalar. The diagonal elements of \mathbf{R}_m are used to represent the resolution. These values range between 0.0 and 1.0, where values close to 1.0 indicate high resolution and, conversely, values near 0.0 indicate poor resolution. Off-diagonal elements in MRM describe the mutual interactions and coupling characteristics among model parameters, reflecting the blending and trade-off relationships of parameter information. This type of coupling fundamentally manifests the non-uniqueness of geophysical inversion. However, extracting and analysing this information generally requires interpretation of the overall structure of the MRM rather than individual elements in practice. Therefore, in this paper, we only focus on the diagonal elements of the MRM. Unless otherwise specified, MRM refers to diagonal elements of the model resolution matrix. In addition, it is important to note that the MRM is applicable only to linear inverse problems in theory. However, under the assumption of the linearization for the nonlinear problems, it can still be applied for model appraisal in ERT (A. Binley & L. Slater 2020).

2.2 Variational inference

In the Bayesian framework, model parameters in inverse problems are converted to a probabilistic posterior pdf. Given the observed data \mathbf{d}_{obs} and model parameters \mathbf{m} , the posterior pdf $p(\mathbf{m}|\mathbf{d}_{\text{obs}})$ is updated according to Bayes' rules

$$p(\mathbf{m}|\mathbf{d}_{\text{obs}}) = \frac{p(\mathbf{d}_{\text{obs}}|\mathbf{m})p(\mathbf{m})}{p(\mathbf{d}_{\text{obs}})}, \quad (9)$$

where $p(\mathbf{m})$ denotes the prior pdf, which represents prior knowledge of the model parameters \mathbf{m} . $p(\mathbf{d}_{\text{obs}}|\mathbf{m})$ is a likelihood that refers to the probability of observed data \mathbf{d}_{obs} given \mathbf{m} . $p(\mathbf{d}_{\text{obs}})$, is the marginal likelihood, also known as the evidence, describing the probability of \mathbf{d}_{obs} integrated over the entire parameter space (M.N. Tran *et al.* 2021), defined as:

$$p(\mathbf{d}_{\text{obs}}) = \int p(\mathbf{d}_{\text{obs}}|\mathbf{m})p(\mathbf{m})d\mathbf{m}. \quad (10)$$

Variational inference estimates the pdf $p(\mathbf{m}|\mathbf{d}_{\text{obs}})$ by replacing the random sampling process in MCMC methods with an approximate optimization. It begins by defining a family of probability distributions $q(\mathbf{m})$, written as $Q = \{q(\mathbf{m})\}$, which is used to approximate the pdf. The optimal approximation $q^*(\mathbf{m})$ is thereafter selected from this family by minimizing a non-negative KL-divergence, which is defined to represent relative entropy, between $q(\mathbf{m})$ and the posterior pdf $p(\mathbf{m}|\mathbf{d}_{\text{obs}})$ (S. Kullback & R.A. Leibler 1951; A. Ganguly &

S.W. Earp 2021). The optimal approximation is given by

$$q^*(\mathbf{m}) = \underset{q(\mathbf{m}) \in \mathcal{Q}}{\operatorname{argmin}} \operatorname{KL}[q(\mathbf{m}) || p(\mathbf{m}|\mathbf{d}_{\text{obs}})], \quad (11)$$

where the KL-divergence is defined as (J. Shlens 2014)

$$\begin{aligned} \operatorname{KL}[q(\mathbf{m}) || p(\mathbf{m}|\mathbf{d}_{\text{obs}})] &= \sum_i q_i(\mathbf{m}) \log \frac{q_i(\mathbf{m})}{p_i(\mathbf{m}|\mathbf{d}_{\text{obs}})} \\ &= \sum_i q_i(\mathbf{m}) \log q_i(\mathbf{m}) - \sum_i q_i(\mathbf{m}) \log p_i(\mathbf{m}|\mathbf{d}_{\text{obs}}) \\ &= E_{q(\mathbf{m})}[\log q(\mathbf{m})] - E_{q(\mathbf{m})}[\log p(\mathbf{m}|\mathbf{d}_{\text{obs}})], \end{aligned} \quad (12)$$

where $E_{q(\mathbf{m})}$ represents the expectation with respect to the distribution $q(\mathbf{m})$. By substituting eq. (9) into eq. (12), the KL-divergence becomes

$$\operatorname{KL}[q(\mathbf{m}) || p(\mathbf{m}|\mathbf{d}_{\text{obs}})] = E_{q(\mathbf{m})}[\log q(\mathbf{m})] - E_{q(\mathbf{m})}[\log p(\mathbf{m}, \mathbf{d}_{\text{obs}})] + \log p(\mathbf{d}_{\text{obs}}), \quad (13)$$

where the former two terms in eq. (13) represent the expectation of the logarithm probability distribution $q(\mathbf{m})$ and logarithm joint distribution $p(\mathbf{m}, \mathbf{d}_{\text{obs}})$ with respect to the distribution $q(\mathbf{m})$, respectively, while the last term represent the logarithm marginal likelihood $p(\mathbf{d}_{\text{obs}})$.

2.3 Stein variational gradient descent

When minimizing eq. (13) using VI, it is essential to select a variational family, such as a simple mean-field variational family (D.M. Blei *et al.* 2017). However, the choice of variational family is critical, as it significantly affects the quality of the posterior (X. Zhang & A. Curtis 2020). To avoid explicit assumptions on variational families, SVGD uses a set of sample distributions (also referred to as ‘particles’), defined as $\{\mathbf{m}_i\}$, to approximate the posterior pdf. In this framework, the target distribution is represented by the density of ‘particles’, which allows for the approximation of complex multimodal posterior distributions. The approximation is achieved by iteratively updating the ‘particles’ through a smooth transform \mathbf{T}

$$\mathbf{T}(\mathbf{m}_i) = \mathbf{m}_i + \varepsilon \Phi(\mathbf{m}_i), \quad (14)$$

where \mathbf{m}_i is the i -th sample distribution in the set $\{\mathbf{m}_i\}$. $\Phi(\mathbf{m}_i)$ is a smooth vector function that indicates the perturbation direction. The scalar ε is the magnitude of the perturbation. The detailed derivations of the SVGD approach can be found in Appendix A. The final optimal direction $\Phi^*(\mathbf{m})$ can be expressed as

$$\Phi_l^*(\mathbf{m}_i^l) = \frac{1}{n} \sum_{j=1}^n \left[k(\mathbf{m}_j^l, \mathbf{m}_i^l) \nabla_{\mathbf{m}_j^l} \log p(\mathbf{m}_j^l | \mathbf{d}_{\text{obs}}) + \nabla_{\mathbf{m}_j^l} k(\mathbf{m}_j^l, \mathbf{m}_i^l) \right], \quad (15)$$

where l and n represent the iteration number and the number of ‘particles’, respectively. $k(\mathbf{m}^l, \mathbf{m})$ is a positive definite kernel (the detailed form will be introduced later). The i -th resistivity distribution \mathbf{m}_i is updated iteratively by $\mathbf{m}_i^{l+1} = \mathbf{m}_i^l + \varepsilon^l \Phi_l^*(\mathbf{m}_i^l)$ until the target RMS is achieved or the iteration converges as conventional ERT inversion.

In eq. (15), the first term (weighted gradient term) primarily serves to drive ‘particles’ towards high-probability regions according to the ERT sensitivity. Therefore, the calculation of the gradient $\nabla_{\mathbf{m}_j^l} \log p(\mathbf{m}_j^l | \mathbf{d}_{\text{obs}})$ in eq. (15) is based on Bayes’ rules (eq. 9) and key to combining ERT with SVGD. It has the following form

$$\nabla_{\mathbf{m}_j^l} \log p(\mathbf{m}_j^l | \mathbf{d}_{\text{obs}}) = \nabla_{\mathbf{m}_j^l} \log p(\mathbf{d}_{\text{obs}} | \mathbf{m}_j^l) + \nabla_{\mathbf{m}_j^l} \log p(\mathbf{m}_j^l), \quad (16)$$

where $\nabla_{\mathbf{m}_j^l} \log p(\mathbf{d}_{\text{obs}} | \mathbf{m}_j^l)$ is the gradient of the log-likelihood and $\nabla_{\mathbf{m}_j^l} \log p(\mathbf{m}_j^l)$ is the gradient of the prior term, which can be treated as a type of implicit regularization of the prior information. In the standard SVGD method, both terms influence the calculation of the SVGD gradient. However, in this paper, we select to use a uniform distribution for both the prior generation and resistivity samplings. In this case, $\nabla_{\mathbf{m}_j^l} \log p(\mathbf{m}_j^l) = 0$, meaning that the prior distribution will not affect the ‘particle’ update and provide no prior information except the boundaries. Therefore, in this work, the SVGD update is effectively driven only by the log-likelihood term.

When assuming that the observational errors are Gaussian distributions, the likelihood $p(\mathbf{d}_{\text{obs}} | \mathbf{m})$ is proportional to $\exp(-\frac{1}{2} \Phi_d(\mathbf{m}))$ (as defined in eq. 3), which is written as (G. Demoment & J. Idier 2008):

$$p(\mathbf{d}_{\text{obs}} | \mathbf{m}) \propto \exp\left(-\frac{1}{2} \Phi_d(\mathbf{m})\right). \quad (17)$$

In this case, the log-likelihood has the following form

$$\log p(\mathbf{d}_{\text{obs}} | \mathbf{m}) = -\frac{1}{2} \Phi_d(\mathbf{m}) + C, \quad (18)$$

where C is a constant. When calculating the gradient of eq. (18) with respect to \mathbf{m}_j^l , the gradient of the log-likelihood is essentially equivalent to the first derivative of eq. (3) with respect to \mathbf{m} , which can be expressed as

$$\nabla_{\mathbf{m}_j^l} \log p(\mathbf{d}_{\text{obs}} | \mathbf{m}_j^l) = \mathbf{J}_{j,l}^T \mathbf{W}_d^T \mathbf{W}_d (\mathbf{d}_{\text{obs}} - \mathbf{d}_{\text{fwd},j,l}), \quad (19)$$

where \mathbf{W}_d , \mathbf{d}_{obs} and $\mathbf{d}_{\text{fwd},j,l}$ are defined as in conventional ERT inversion (see eq. 6). $\mathbf{J}_{j,l}$ is the Jacobian matrix of $\mathbf{d}_{\text{fwd},j,l}$ with respect to \mathbf{m}_j^l . Here, we also use the logarithm of resistivity to represent the subsurface properties. Therefore, \mathbf{m}_j^l denotes the logarithm of the resistivity and $\mathbf{J}_{j,l}$ represents the Jacobian matrix of the transfer resistance with respect to the logarithm of resistivity.

The second term in eq. (15), known as the ‘repulsive term’, which is used to push ‘particles’ away from each other and thereby avoiding collapsing into a single mode (X. Zhang *et al.* 2021). The kernel $k(\mathbf{m}_j^l, \mathbf{m}_i^l)$ in these two terms provides the interaction intensity between ‘particle’ pairs according to their mutual distance and eventually contributes to the balance between the ‘weighted gradient term’ and ‘repulsive term’. In this paper, we use a gradient matrix-valued kernel $k(\mathbf{m}_j^l, \mathbf{m}_i^l)$ for eq. (15), defined as (X. Zhang & A. Curtis 2024a)

$$k(\mathbf{m}_j^l, \mathbf{m}_i^l) = \mathbf{D}^{-1} \exp \left[-\frac{\|\mathbf{m}_j^l - \mathbf{m}_i^l\|_{\mathbf{D}}^2}{2h^2} \right], \quad (20)$$

where h is a bandwidth parameter and satisfies $h = \text{med}^2 / \log n$, where med represents the median of distances between all pairs of ‘particles’ to balance the gradient of each particle against the influence from others (Q. Liu 2017). \mathbf{D} is a positive definite diagonal matrix, constructed similar to an optimization algorithm AdaGrad (J. Duchi *et al.* 2011; X. Zhang & A. Curtis 2024a) commonly used in machine learning, defined by:

$$\mathbf{D}^{-1} = \frac{1}{\sqrt{\mathbf{v}_i^2}}, \quad (21)$$

where \mathbf{v}_i^2 is an accumulated squared gradient, with the following form

$$\mathbf{v}_i^2 = (1 - \beta) \mathbf{E}_i(\mathbf{g}_i^2) + \beta \mathbf{v}_{i-1}^2, \quad (22)$$

$$\mathbf{E}_i(\mathbf{g}_i^2) = \frac{1}{n} \sum_{i=1}^n \mathbf{g}_{i,i}^2, \quad (23)$$

where β is a learning rate, which defaults to 0.95. \mathbf{g}_i is an instantaneous gradient at iteration l , which equals $\mathbf{J}_i^T \mathbf{W}_d^T \mathbf{W}_d (\mathbf{d}_{\text{obs}} - \mathbf{d}_{\text{fwd},i})$.

3 SYNTHETIC EXPERIMENTS AND RESULTS

3.1 Synthetic experiment on the effect of electrode configurations

A synthetic block model (Fig. 2a) was constructed to simulate a resistivity anomaly that may be associated with, for example, localized groundwater contamination and to evaluate the performance of the SVGD method. The block anomaly measures 4 m × 6 m and has a resistivity of 10 Ωm, while the background resistivity is 100 Ωm. To explore the effects of two different electrode configurations [Dipole–Dipole (DD) and Wenner–Schlumberger (WS)] an electrode array with a total of 50 electrodes at 1 m spacing was used. The configurations modeled consisted of the maximum number of voltage dipole spacings (a) possible, and the factor n (dipole separation, see e.g. A. Binley & L. Slater 2020) was set to be 1, 2 and 3, resulting in 905 and 1085 measurements for the DD and WS arrays, respectively. To simulate field conditions contaminated by noise, 1 per cent Gaussian noise was added to the synthetic data. This noise level was also treated as the prior data weight parameter b (eq. 5) in the inversion.

In SVGD, the prior distribution of the base 10 logarithm resistivity was defined as a Uniform distribution between 0 and 3 (\log_{10} resistivity in units of Ωm). This range ensures that the prior not only contains the resistivity value of the true model, but also allows ‘particles’ to explore a broader parameter space beyond the core region. An analysis using different ‘particle’ numbers (400, 800 and 1200) is reported in Fig. S1 (Supplementary Information) and the computational time is shown in Table S1 (Supplementary Information). To balance accuracy and computational efficiency, the number of ‘particles’ was set to be 800. This choice is also comparable to the range of 400–800 ‘particles’ widely used in seismic VI (X. Zhang & A. Curtis 2020, 2021; X. Zhang *et al.* 2023). Increasing the number of ‘particles’ does not necessarily improve inversion performance but obviously increases computational cost and the number of iterations (J.Y. Zhang *et al.* 2020), which may be impractical for application of the method. The initial average RMS of all ‘particles’ are 60.56 (DD array) and 61.48 (WS array). The inference process was considered converged once the RMS error reached the pre-defined target value of 1.0. Upon convergence, 800 sample resistivity distributions were obtained for synthetic data. These distributions were then used to estimate the posterior distributions (sample mean) and associated uncertainties, such as standard deviation (STD), based on statistical analysis. For comparison, a conventional inversion with model appraisal was also carried out using the code R2 (A. Binley & L. Slater 2020), which produced both inverted resistivity images and their MRM. Since the Gaussian–Newton method is a deterministic inversion approach, which requires an explicit initial model, a uniform background resistivity of 100 Ωm was used in this experiment. In addition, it is worth noting that different methods for constructing kernel $k(\mathbf{m}_j^l, \mathbf{m}_i^l)$, such as radial basis function

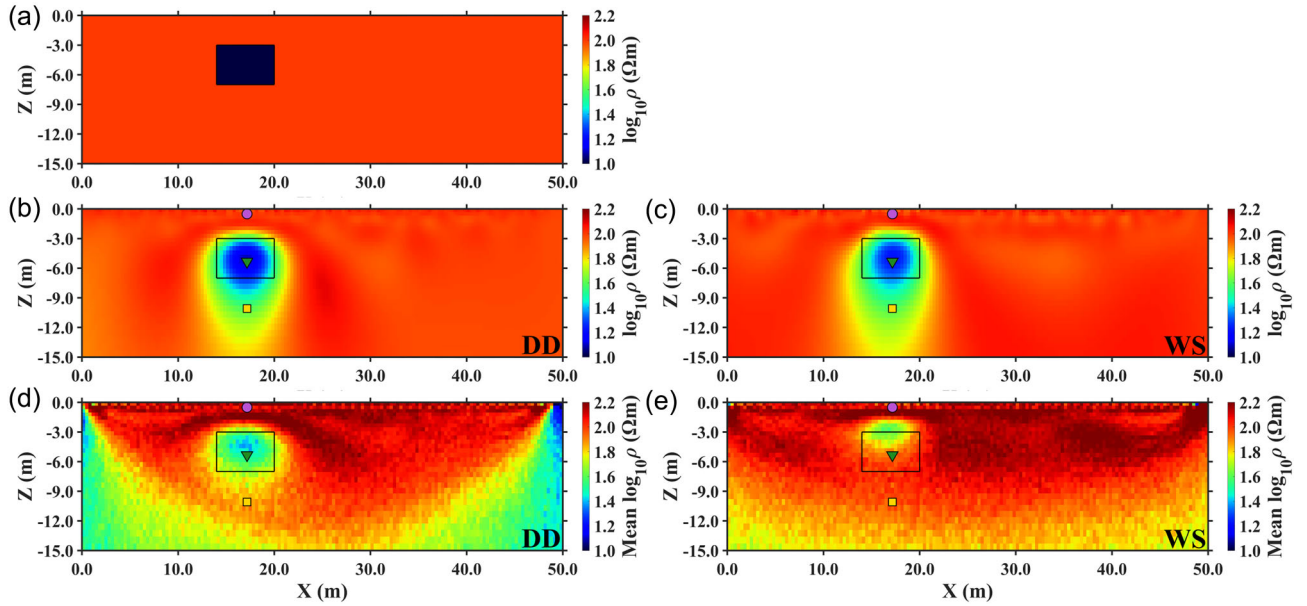


Figure 2. The synthetic model and resistivity images obtained from R2 and SVGD. (a) The true block model; (b, c) inverted resistivity images from R2 using DD and WS arrays, respectively; (d, e) sample mean resistivity images from SVGD using DD and WS arrays, respectively. The three symbols in panels (b)–(e) indicate locations of the selected points to show posterior resistivity probability distributions in Fig. 4.

(RBF) kernel (C.E. Rasmussen & C.K.I. Williams 2005) or variance matrix-valued kernel (X. Zhang & A. Curtis 2021), can produce different results. An experiment was conducted using different kernels, as shown in Fig. S2 and Table S2 (Supplementary Information). Compared with RBF or variance kernel, the Jacobian matrix is intergrated into gradient kernel, therefore, it has a stronger capacity to reflect the characteristics of sensitivity and converges more readily, therefore, it performs better in low-resolution regions. Therefore, all the experiments are based on gradient kernel in this paper.

Figs 2(b)–(e) show the inverted resistivity images from R2 and the sample means from SVGD. Overall, the results from the DD array are better than those from the WS array. This is attributed to the, expected, stronger anomaly sensitivity of the DD array to the low-resistivity target body (e.g. T. Dahlin & B. Zhou 2004). R2 successfully recovers the block structure using both arrays, although artifacts appear beneath the block due to the smoothness constraint imposed during inversion. Similarly, SVGD also captures the block structure with the DD array, although the inverted sample mean resistivity is slightly higher than the true value. However, the result of the SVGD using the WS array fails to reconstruct the true model perfectly—only the upper region of the anomaly target is resolved in the sample mean.

A clear detection depth scale (i.e. depth of investigation) is revealed in the SVGD sample mean using the DD array, and extends deeper when using the WS array. In contrast, such detection scales are not shown in the R2 inverted images—this is caused by the high regularization. In Gauss–Newton based inversion, regularization is essential for stabilizing the ill-conditioned geophysical inverse problems (A. Binley & L. Slater 2020). However, in regions with low-data sensitivity, the inversion is dominated by the regularization term, resulting in artificially smooth resistivity distributions and masking the detection scale. In contrast, SVGD does not rely on spatial regularization for updating ‘particles’. The ‘particles’ located beyond the detection scale are only minimally updated due to poor sensitivity, resulting in mean values close to the prior mean. The SVGD method can, therefore, identify the detection scale well. Note that sample means out of the detection scale are dependent on the prior distributions—different sample means will be recovered when applying different prior distributions. In this case, a theoretical STD (e.g. about 0.866 for uniform prior between 0 and 3) may be useful to quantify the regions out of the detection scale in SVGD. Additionally, the artifacts caused by smooth regularization are reduced in the sample mean from SVGD, as shown in Figs 2(b) and (d). Nevertheless, high-resistivity artifacts appear in the upper portion of the SVGD sample means, which is reduced by the spatial regularization in conventional inversion. Similar phenomenon has also been observed in VI for traveltimes data, which orientates from data overfitting using a fixed regular grid of elements (X. Zhang & A. Curtis 2020). In this case, these two methods present their respective advantages and disadvantages in terms of artifacts—the differences between these two methods in low-sensitivity regions stem from their inherent assumptions and mathematical mechanisms: R2 tends to maintain model smoothness through regularization, while SVGD reflects prior-dominated model uncertainty when lacking data constraints. Understanding these differences helps to correctly interpret the inversion results.

Figs 3(a)–(d) illustrate the STD and MRM for model appraisal. Both approaches present some similarities, specifically, lower uncertainty in the shallow subsurface and significantly higher uncertainty at greater depths. However, there are some differences in the region of the low-resistivity anomaly. In the MRM results (Figs 3a and b), the block region exhibits slightly lower resolution values than the surrounding background at the same depth, whereas the STD from SVGD is slightly higher in the block region. Comparing

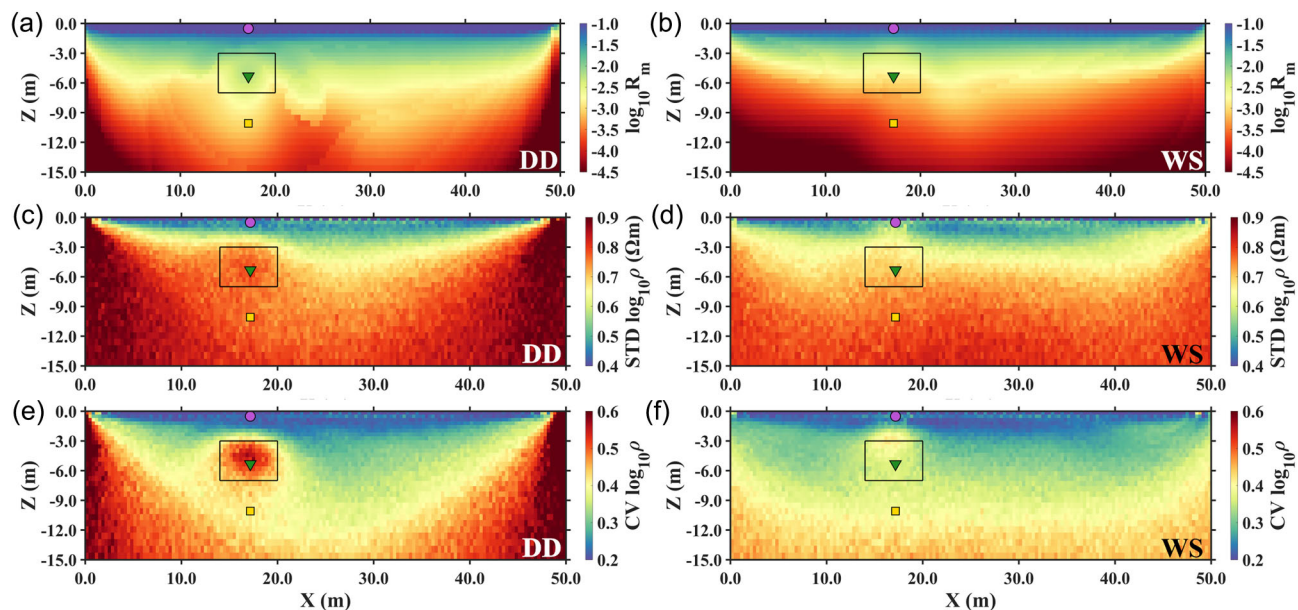


Figure 3. Model appraisal of resistivity images using the DD and WS arrays, respectively. (a, b) The MRM from R2; (c, d) the STD from SVGD; (e, f) the CV from SVGD.

the two different configurations, the DD array produces high MRM in the block region, indicating high resolution, whereas the WS array shows relatively high-MRM values in the upper half of the block but lower values in the lower half, implying that the results in the upper part of the block is more reliable than that in the lower part. Referring back to the sample mean of the WS array in Fig. 2(e), this explains the reasons for the failure to resolve the anomaly in the lower half of the block. Due to limited resolution of the WS array in the lower part, the data lack sufficient resolution to recover the structure at that part. The different imaging effects across different regions can be more clearly demonstrated and illustrated through the model validation in Section 4.2. In contrast, the conventional inversion using R2 reveals a larger anomaly (Fig. 2c), which is simply a result of smoothing (regularization) and clearly not because of measurement sensitivity.

Using the STD alone to capture the specific uncertainty associated with the block may be limited. This is because the STD primarily reflects absolute uncertainty that varies with depth from the configurations rather than the anomalies. Therefore, to better present the relative uncertainty in the anomalies, the coefficient of variation (CV) may be more useful. The CV is defined as the ratio of the STD to the sample mean, as follows

$$CV = \frac{\sigma}{\mu}, \quad (24)$$

where σ and μ denote the STD and the sample mean, respectively. As shown in Fig. 3, a relatively high CV is observed in the block in the DD array, although a high-CV region is observed only in the upper half of the block for the WS array. Note that the high-CV values shown in Fig. 3 are specific to the low-resistivity block model. Different subsurface resistivity structures may produce different CV patterns due to variations in the sample mean. Nevertheless, the CV may be an effective way to represent the relative uncertainty. Recall that we are posing this example as one not unlike the problem of anomaly detection due to groundwater contamination. Being able to quantify the uncertainty in the geoelectrical model would potentially add immense value to the overall assessment of a site.

In Fig. 4, we present three posterior resistivity probability distributions at specific points: Near the surface, in the block and beneath the block, as indicated in Fig. 3. These distributions reveal examples of non-Gaussian behavior—some exhibit complex multimodal distributions. As shown in Figs 4(a) and (d), the resistivity distributions display local peaks around $\log_{10}(\rho) = 2$, indicating a concentration of inferred values close to the background ($100 \Omega\text{m}$). For the location within the block (Figs 4b and e), the distributions show a wide range of resistivity values, which is consistent with the high STD observed in Fig. 3. This feature reflects the non-uniqueness of geophysical inversion: Multiple combinations of resistivity values and shapes can equally fit the same observed data; it reveals a trade-off between the anomaly resistivity and associated shapes (E. Galetti *et al.* 2015; X. Zhang *et al.* 2018), which is not well resolved by the diagonal elements in MRM. For the deepest points in Figs 4(c) and (f), the distributions appear close to the prior, caused by the poor sensitivity at these depths.

A tailing effect is observed in some of the distributions shown in Fig. 4, that is, resistivity values cluster near the upper boundary of the prior range. This may originate from the limitations of the uniform prior distribution. During the sampling process, a range is pre-defined so that resistivity sampled outside the boundaries is shifted back to the range to remain consistent with the prior information. However, this can be critical because ERT has reduced sensitivity to high-resistivity structures (A. Binley & L. Slater 2020). Setting overly broad boundaries on resistivity (i.e. the prior range) may lead to an excessive concentration of ‘particles’ in unphysical

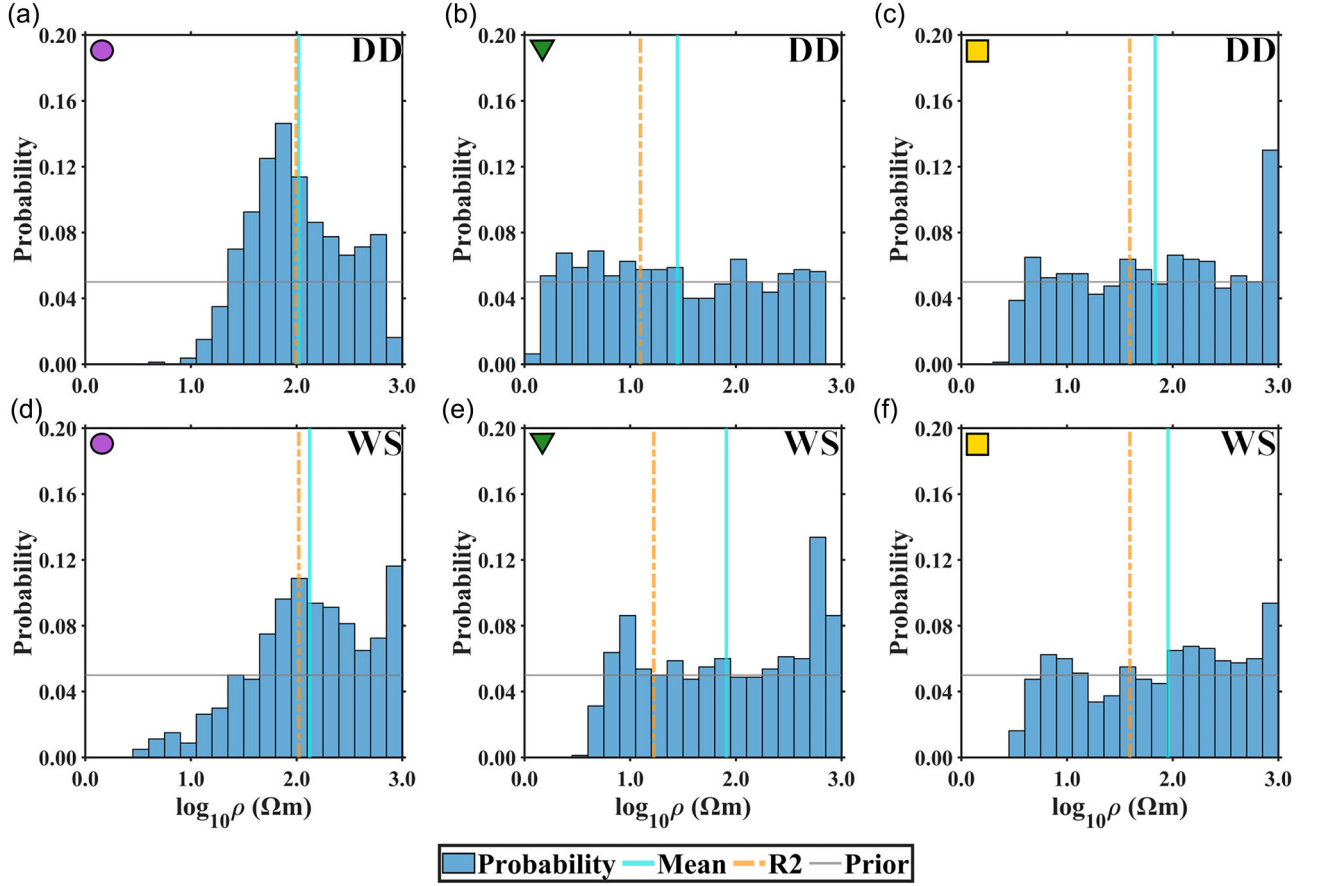


Figure 4. Posterior resistivity probability distributions at the selected points in Fig. 2. (a–c) for the DD array; (d–f) for the WS array. The cyan and brown lines represent the sample mean from SVGD and the inverted resistivity from R2, respectively. The grey horizontal lines represent the prior resistivity distributions.

high-resistivity regions, which can potentially increase the number of required ‘particles’ and raise computational costs. Therefore, a reasonable range needs to be given according to the geological conditions, which somewhat reflects the importance of the given prior information (A. Curtis & A. Lomax 2001). Some other distributions, such as Gaussian distribution (X.B. Zhao & A. Curtis 2024a) and Cauchy distribution (W. Alemie & M.D. Sacchi 2011), may produce different results by influencing the gradient of the prior term $\nabla_{\mathbf{m}_j} \log p(\mathbf{m}_j^l)$. For instance, if a Gaussian prior $\mathbf{m}_j^l \sim \mathcal{N}(\mu, \sigma^2)$ is used, $\nabla_{\mathbf{m}_j^l} \log p(\mathbf{m}_j^l) = -\frac{1}{\sigma^2}(\mathbf{m}_j^l - \mu)$, contributes directly to the update. This implies that the gradient term exerts a ‘pull’, attracting each ‘particle’ towards the prior mean. This has the possibility of reducing the ‘tail effect’ but specifying an appropriate prior mean introduces a new challenge, which warrants future investigation.

A further characteristic to note is that the lack of symmetry in some of the distributions highlights that the use of simple statistics (mean, standard deviation) may be misleading. We explore this further in a later example.

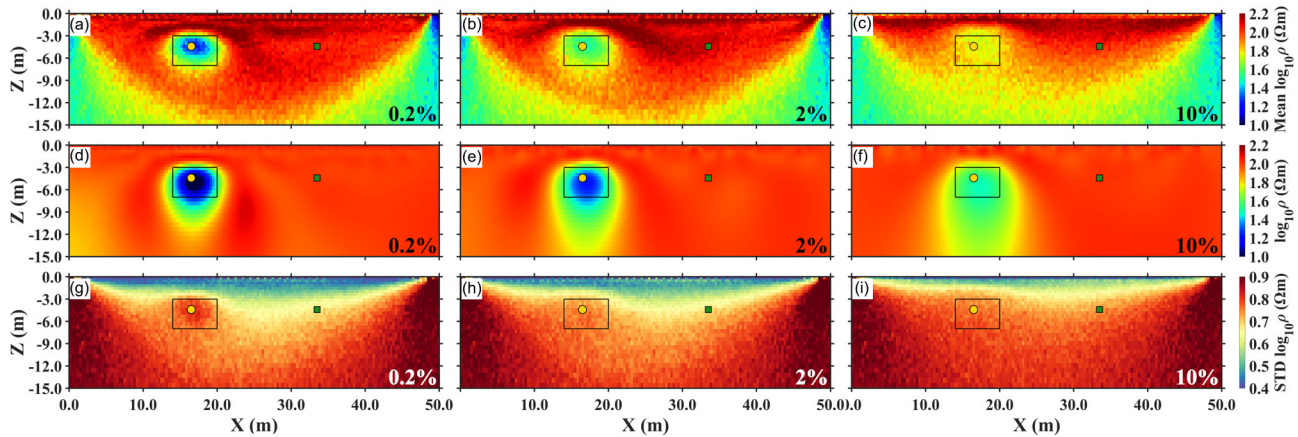
3.2 Synthetic experiment on the effect of noise

In this section, we continue to use the block model to study the uncertainty due to measurement noise. We tested the synthetic data using DD array with Gaussian noise levels of 0.2, 0.5, 1.0, 2.0, 3.0, 4.0, 5.0, 7.5, 10, 15 and 20 per cent. When a very small noise level (less than 2 per cent) is used, the term $\nabla_{\mathbf{m}_j} \log p(\mathbf{d}_{\text{obs}} | \mathbf{m}_j^l)$ in eq. (19) becomes very large, which may cause the iterative process to be destabilized by a very large ‘particle’ update step. Therefore, for noise levels less than 2 per cent, we fixed the prior data weight b to 0.02 and adjusted the target RMS values accordingly. For example, the target RMS value of a 0.2 per cent Gaussian noise experiment was reduced to 0.1 with an assumed weight b of 0.02. For noise levels above 2 per cent, we used the corresponding noise levels for the data weight calculation.

The computational times for different noise levels were summarized in Table 1. All computations were performed on a workstation equipped with an Intel Core i9-13900HX processor using 20 threads in SVGD and 1 thread in R2. The computation time of R2 depends on the number of iterations and the choice of step size during the inversion process, but most calculations together with MRM complete within 10–12 min. For SVGD, each iteration requires roughly the same amount of time, not exceeding 4 min for the 905 measurement and the inversion mesh of 6630 elements. For noise levels between 2 and 10 per cent, the algorithm can reach the target RMS within 100

Table 1. The iteration numbers and computational time for different noise levels. ‘*’ denotes solution converged to the target RMS 1.1 rather than 1.0.

Noise levels	SVGD iteration number	SVGD computational time (s)	SVGD computational time/iteration (s)	R2 computational time including MRM (s)
0.2 per cent	381	80 864	212	662
0.5 per cent	186	38 451	207	713
1.0 per cent	137	28 135	205	647
2.0 per cent	97	21 791	225	640
3.0 per cent	91	20 032	213	705
4.0 per cent	92	20 238	220	718
5.0 per cent	90	19 689	219	862
7.5 per cent	93	20 697	223	634
10 per cent	95	21 026	221	1073
15 per cent	106	22 558	213	656
20 per cent	128	28 579	223	740*

**Figure 5.** The sample mean and STD from SVGD, and inverted resistivity from R2 for three noise levels: 0.2, 2 and 10 per cent, respectively. (a–c) The sample mean resistivity from SVGD; (d–f) the inverted resistivity from R2; (g–i) the STD from SVGD. The circle and square indicate the two representative points selected to analyse STD variations.

iterations, while it needs more iterations for noise out of this range. For noise levels below 2 per cent, SVGD requires more iterations to reach the target RMS due to excessively large jumps and oscillate during ‘particle’ updates. For noise levels more than 10 per cent, the resolution is quite limited and hard to support accurate ‘particle’ updates, which leads to a need for many more iterations to reach the target RMS. Nevertheless, such low- or high-noise levels are typically used only in synthetic examples rather than in field data. Therefore, this method appears practical for application in 2-D ERT imaging. 3-D ERT inversion using SVGD requires substantially more computational time. Possible approaches to addressing this challenge are proposed in the Discussion section.

To illustrate the impact of noise levels, we selected three experiments (0.2, 2 and 10 per cent) and present related sample mean and STD from SVGD, and inverted resistivity images from R2, as shown in Fig. 5. The comparison between the sample means and inverted resistivity images at different noise levels indicates that the resolution of the low-resistivity block decreases with increasing noise levels. Figs 5(a)–(c) show that the overall shape of the anomaly has not changed significantly based on the sample mean, although the mean resistivity value tends to approach the background resistivity due to the reduced resolution. However, Figs 5(d)–(f) reveal that the extent of artifacts beneath the block expands with increasing noise levels. This suggests that, under high-noise levels, the inversion process becomes increasingly dependent on regularization and the results may reflect more about the assumed model structure rather than the anomaly sensitivity of the data.

Two locations (Fig. 5) are selected to study the uncertainty variation of the anomaly and background. These two points are at the same depths and symmetrical relative to the electrode array, thus minimizing the effect of geometry in the measurement configurations. The STD variations of these two points across different noise levels are illustrated in Fig. 6. For the background location (green square in Fig. 5), the STD increases continuously with increasing noise levels. This trend is consistent with expectations, as higher noise levels naturally lead to greater uncertainty. However, for the location within the block (yellow circle in Fig. 5), the STD exhibits a non-monotonic behaviour: It decreases as the noise level increases to about 4 per cent but then increases when the noise level is greater than about 4 per cent. This suggests the presence of a potential factor influencing the STD in this location. Since the influence of the configurations and depth was excluded when selecting observation points, this potential factor likely originates from the anomaly itself. As discussed above, the anomaly effect is determined by both shape (geometry) and associated resistivity, both of which contribute to the uncertainty at that location. However, the presence of noise can reduce the resolution of an anomaly, thereby suppressing its effect. At low noise levels, the effect of the anomaly dominates, and a high STD primarily reflects the trade-off between shape and

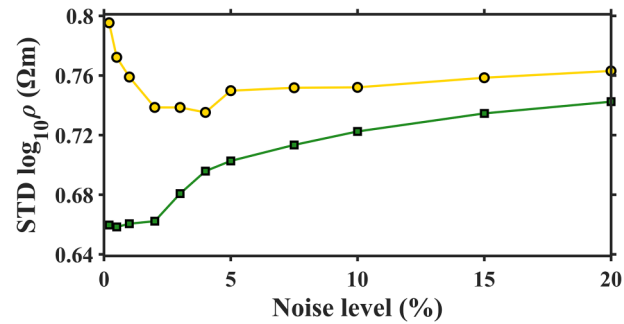


Figure 6. The STD variations at the circle and square points (in Fig. 5) across different noise levels.

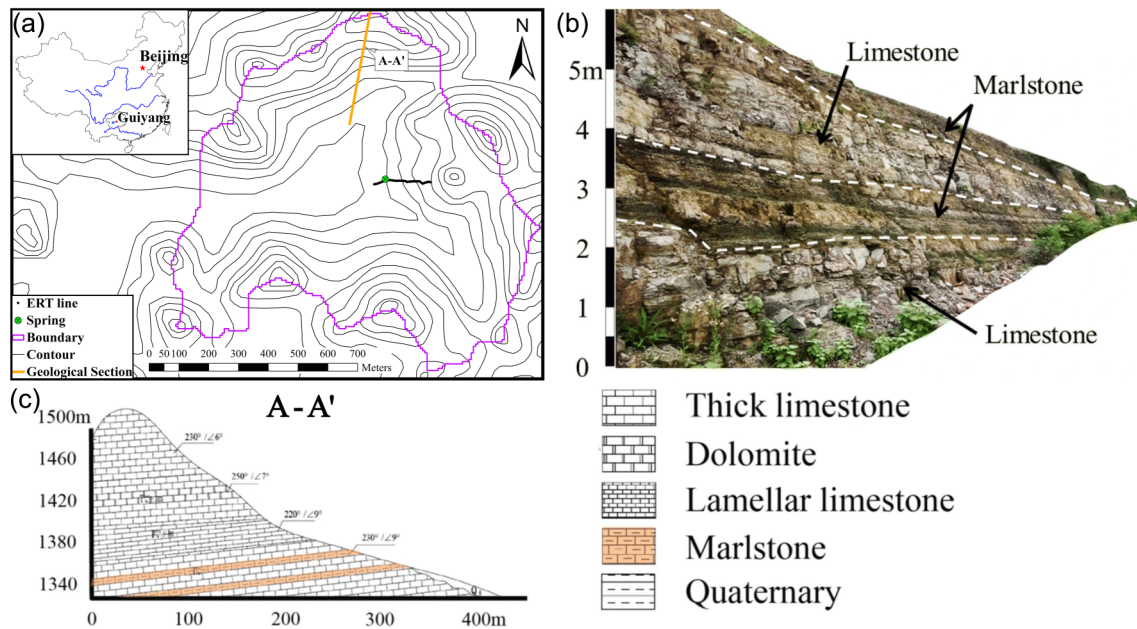


Figure 7. Geographical and geological description of the Chenqi watershed. (a) Geographical map and the location of ERT survey line; (b) outcrop in the Chenqi watershed; (c) A–A' geological profile (modified from Q. Cheng *et al.* 2019).

resistivity rather than noise effects. As the noise level increases, the STD decreases due to the diminishing influence of the anomaly. However, when noise becomes so high that the sensitivity of the data to the anomaly is weak, the STD follows a similar trend to that in the background region. It is worth noting that although noise effects are dominant, anomaly effects still exist when inverting, therefore uncertainty remains slightly higher than in the background until the noise level is so high that data from the anomaly region are indistinguishable from those in the background (i.e. the two lines in Fig. 6 would converge).

Despite the experiment highlighting the balance between anomaly and noise effects, the STD does not vary significantly across different noise levels considered in Fig. 6, with a maximum increase of 12.5 per cent at the green point and a maximum decrease of 7.6 per cent at the yellow point. It indicates that the effect of depth on the resolution of ERT may be more dominant than the balance between anomaly and noise effects. It is worth noting that the sample STD is determined based on the ‘particle’ distribution. Therefore, factors that influence the ‘particle’ distribution, such as the construction of the kernel $k(\mathbf{m}_j^t, \mathbf{m}_i^t)$ in eq. (20) and the prior distribution, may potentially affect the observed noise effect, which warrants further investigation.

4 FIELD EXPERIMENT AND MODEL VALIDATION

4.1 Field experiment in the Chenqi watershed

A field data set collected in a small Chenqi subcatchment (Fig. 7a) in the Houzhai watershed in Guizhou Province, China was used to illustrate the practical benefits of the quantified resistivity probabilities and uncertainties through VI in field data. Chenqi has a classical cockpit karst landform; the hydrological characteristics of the subcatchment have been studied extensively (e.g. X. Chen *et al.* 2018). These studies have revealed complex dynamic behaviour due to contrasting subsurface hydrogeological units, highlighting the potential value of hydrogeophysical investigations. Within Chenqi four types of rocks are exposed: limestone, dolomite, lamellar

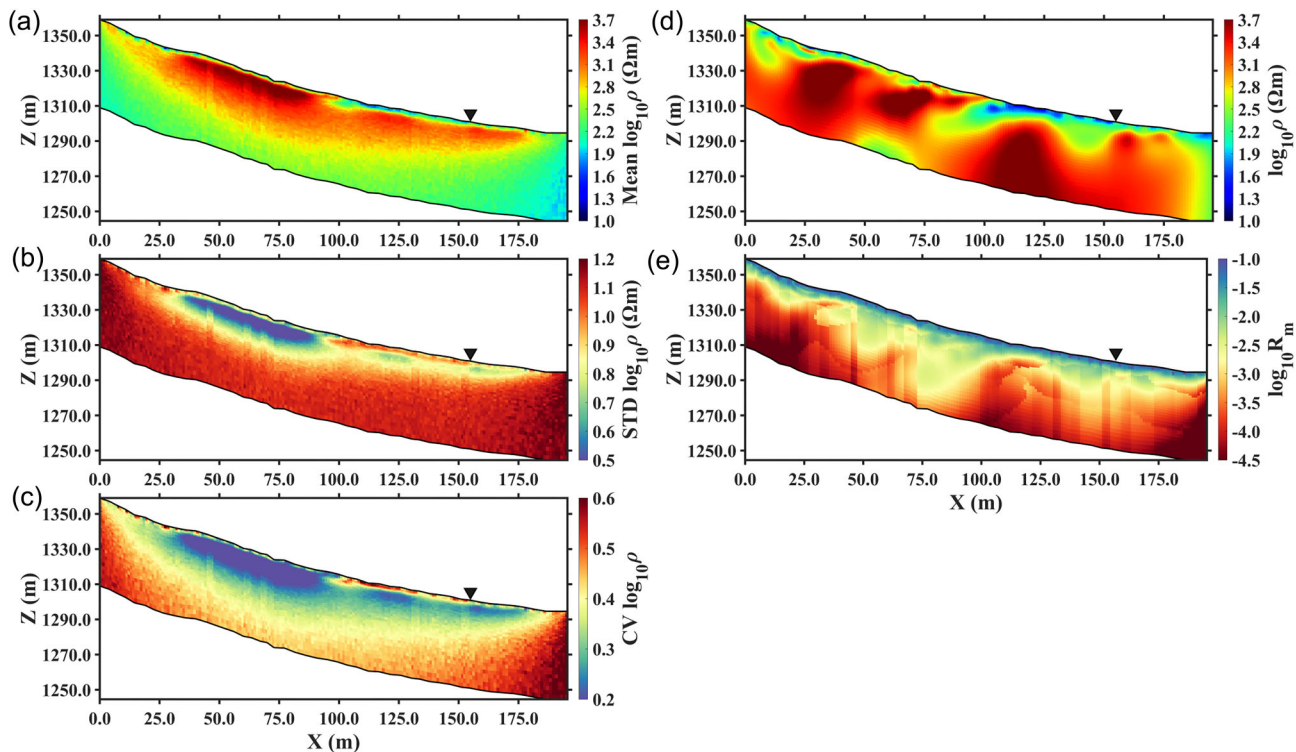


Figure 8. Inverted resistivity results and model appraisal for the field data. (a–c) Sample mean, STD and CV of the field data from SVGD, respectively; (d, e) inverted resistivity image and its MRM from R2. The black triangle in each image shows the location of the spring.

limestone and marlstone, exhibiting a nearly horizontal, layered sedimentary structure, as shown in Figs 7(b) and (c). Q. Cheng *et al.* (2019) carried out an extensive geophysical investigation of Chenqi using ERT based on a conventional inversion approach. In one of the hillslopes covered by Q. Cheng *et al.* (2019), a near-surface wedge-shaped low-resistivity zone was argued to give evidence of a marlstone layer, which, in turn, suggested a mechanism for driving significant spring flow observed on the hillslope. However, Q. Cheng *et al.* (2019) did not provide evidence that the marlstone layer extended within the hillslope given the limited resolution of ERT at depth. We reanalyse one of the data sets from the study of Q. Cheng *et al.* (2019), a survey line different from that reported in C.H.M. Tso *et al.* (2021), to assess the uncertainty in resistivity contrast due to this marlstone layer. The dataset consists of 1963 measurements in DD configuration using a 48 electrode array, with 5 m spacing. Measurements were made with a dipole spacing of 5, 10 and 15 m.

To investigate the apparent absence of the low-resistivity marlstone at depth, we reprocessed the field data using VI and compared the results with the resistivity images inverted by R2. In this experiment, as before, we used 800 ‘particles’ with a prior uniform logarithmic distribution ranging from 0 and 4 (units of $\log_{10} \Omega\text{m}$). The data weight coefficients (eq. 5) a and b were set to 0.001 Ω and 0.05, respectively, which is roughly equivalent to a 5 per cent noise level.

A comparison of these two methods applied to the field data is shown in Fig. 8. Both results in Figs 8(a) and (d) reveal a pattern of low resistivity near the surface and higher resistivity at greater depths. However, the near-surface low-resistivity layer using VI (Fig. 8a) appears much shallower, with a sharper boundary between the low- and high-resistivity zones compared to the R2 inversion (Fig. 8d). The difference is caused by the removal of the smoothness regularization, as demonstrated in the synthetic experiments earlier. Regarding the wedge-shaped low-resistivity feature [interpreted by Q. Cheng *et al.* (2019) to be a consequence of a marlstone layer], the two images exhibit completely different results. The sample mean resistivity from VI (Fig. 8a) does not indicate that the marlstone extends to greater depths, but note that the STD image (Fig. 8b) indicates a high level of uncertainty. In contrast, the resistivity image from R2 appears to show that low-resistivity marlstone extends downwards between $X = 75$ m and $X = 100$ m. Additionally, the MRM (Fig. 8e) in this region is also relatively higher than the surrounding regions, further supporting the reliability of this feature in the R2 results. However, it is important to recognize that the MRM only reflects uncertainty specific to the inverted image. Due to the non-uniqueness of the geophysical inversion, the inverted optimal resistivity cannot fully represent the true model although it may be the most probably solution from the optimization. Moreover, as shown in the synthetic experiment in Fig. 2, detecting low-resistivity structures in a high-resistivity background can lead to artifacts beneath the anomalies. Therefore, further analysis is required to evaluate the reliability of these interpretations in the next section.

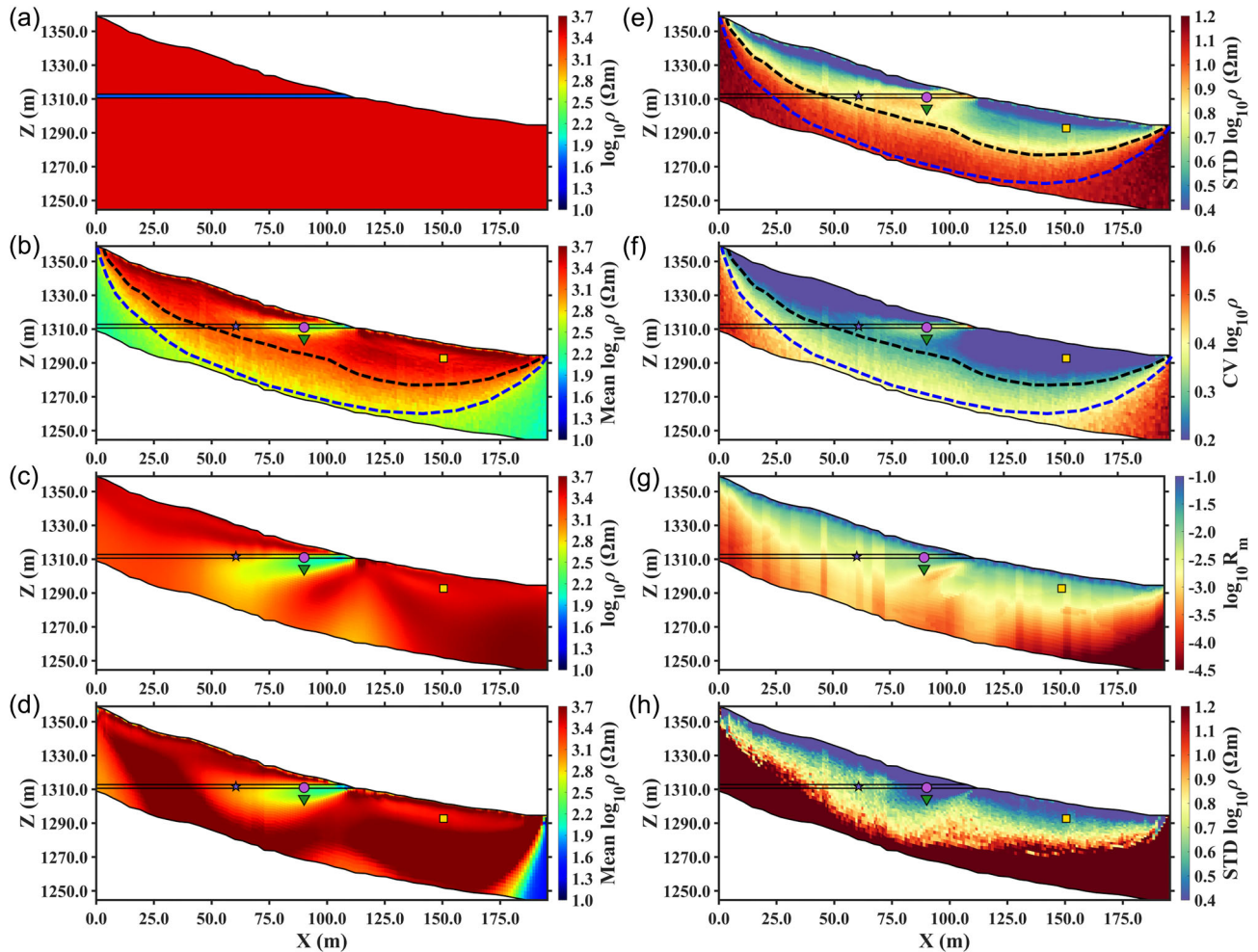


Figure 9. Synthetic model validation for the Chenqi watershed. (a) The synthetic model of the limestone and marlstone; (b–d) the sample mean and inverted resistivity image from SVGD, R2 and ADVI, respectively; (e, f) the STD and CV from SVGD, respectively; (g) the MRM from R2; (h) the STD from ADVI. The black solid lines represent the true boundaries between limestone and marlstone. The two dotted lines represent the boundaries inferred according to the STD and sample mean from SVGD, respectively. The symbols are the representative points selected to show the resistivity distributions in Fig. 10.

4.2 Model validation for field data

In the absence of independent geological or hydrogeological information to constrain the subsurface structure, we adopted a model validation approach to investigate the influence of marlstone, following the methodology of Q. Cheng *et al.* (2019). A synthetic model was constructed based on idealized geological conditions, as illustrated in Fig. 9(a). In this model, a low-resistivity layer with a resistivity of $50 \Omega\text{m}$ and a thickness of 2.2 m represents the marlstone, while the surrounding high-resistivity background is set to be $3000 \Omega\text{m}$ to represent the limestone. The same measurement configurations as used in the field data set was adopted. A forward model was generated and 5 per cent Gaussian noise was added to these data.

A comparison of inversions using SVGD, R2 and ADVI is presented in Fig. 9. The principles of ADVI approach are described in X. Zhang & A. Curtis (2020). In this section, we still use 800 ‘particles’ for both the ADVI and SVGD methods. In SVGD, the prior distribution was defined as a uniform distribution between 0 and 4; while in ADVI, the prior distribution was defined as a Gaussian distribution with a mean of 2 and an STD of 0.5, ensuring over 99.99 per cent of the samples fall within the range between 0 and 4 (both distributions are defined in terms of the base 10 logarithm resistivity). Comparing sample means and inverted resistivity, R2 and ADVI provide similar resistivity patterns, whereas SVGD yields different result. This phenomenon stems from the basic that applying spatial regularization using the L2 norm (Tikhonov regularization) is equivalent to employing a Gaussian prior in Bayesian inference (J.C. Chang *et al.* 2014). It is evident that the anomaly due to the synthetic marlstone is sharper in sample mean from SVGD (Fig. 9b) compared to the more traditional regularized gradient-based inversion using R2 and probabilistic inversion using ADVI (Figs 9c and d). Also note in Figs 9(c) and (d) that the centre axis of the anomaly clearly deviates from (true) horizontal orientation, giving the illusion that the low-resistivity layer extends diagonally downwards. The MRM from R2 and the STD from ADVI indicate a high resolution in the region of the marlstone layer but also a relatively low resolution beneath it; this pattern is consistent with the field data shown in

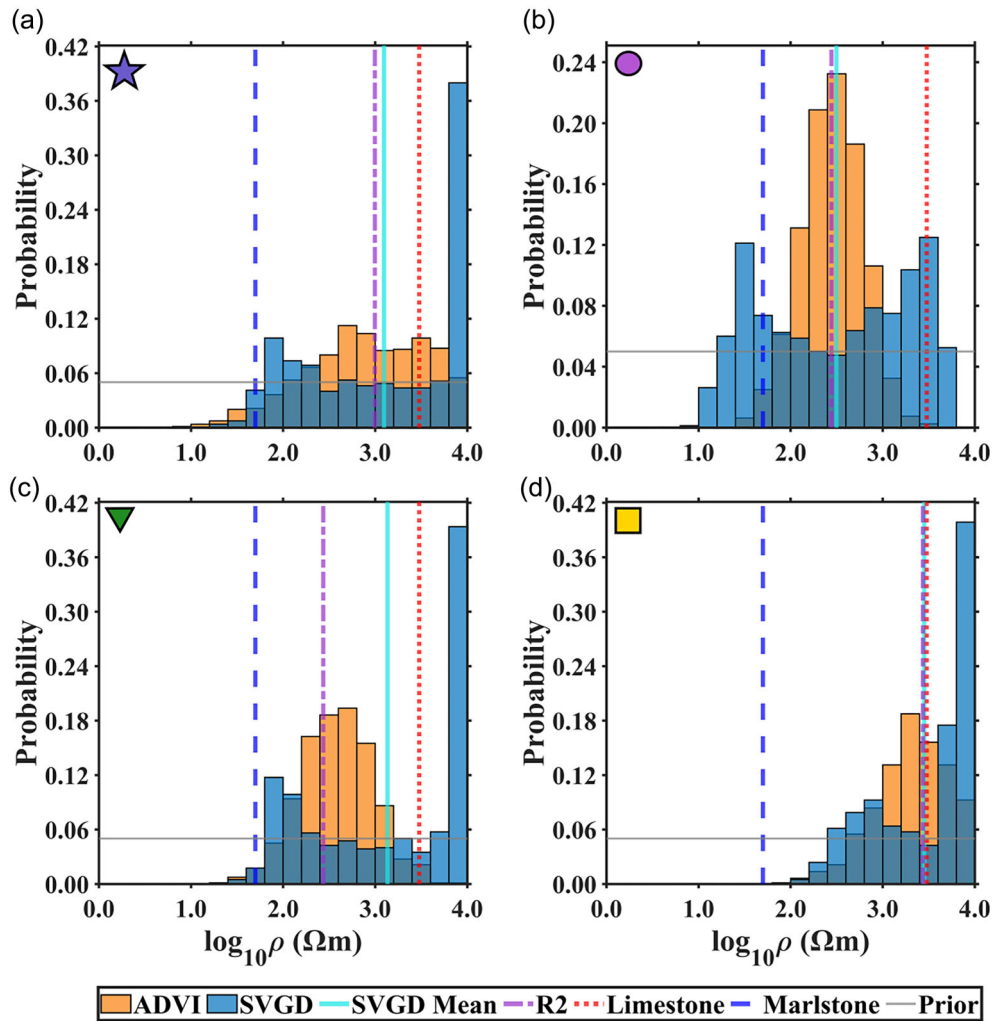


Figure 10. Posterior probability distributions of the SVGD and ADVI at the selected points in Fig. 9. The cyan and purple lines represent the inverted resistivity or the sample mean obtained from R2 or SVGD, respectively. The blue and red lines represent the true marlstone and limestone, respectively. The grey horizontal line represents the prior distribution.

Fig. 8(e). This suggests that the apparent downward extension of the low-resistivity structure in the inverted field dataset (Fig. 8d) is an artifact generated by the smooth regularization or the assumption of Gaussian prior. In contrast, the limestone region is shown with a high-sample mean with a low STD, while the marlstone has a low-sample mean with a high STD in Figs 9(b) and (e), which aligns well with the field data in Figs 8(a) and (b). This correspondence confirms that the uncertainties between the synthetic and field data follow the same patterns, thereby motivating the following analysis about the resolution boundaries.

Two different boundaries are marked by broken lines in the SVGD results shown in Figs 9(b), (e) and (f). The (lower) blue boundary indicates a depth of inversion: Beyond this boundary the sample mean is apparently unaffected by the data. The (shallower) black boundary indicates a transition from low to high STD. The area between these two boundaries is interpreted as a region where a transition from high to low resolution occurs. Furthermore, as shown in Fig. 9(e), a layer of high-STD layer is clearly evident. In the high-resolution region, the low-resistivity marlstone is recovered due to sufficient sensitivity of the measurements. Although the low-resolution region can still provide some information about the background, as indicated in Fig. 9(b), it lacks the capability to reliably recover the marlstone feature. Similarly, in the field experiment, the marlstone with high uncertainty is also near this boundary, as shown in Fig. 8(b). This limitation is the primary reason why the downward extension of the low-resistivity marlstone is not observed in the inverted field data.

We selected four representative points (see Fig. 9) to analyse the posterior resistivity distributions from the SVGD and ADVI approaches and compare with the values derived by R2. Two of these points are located in the marlstone, with one near the surface and the other one near the boundary of the high- and low-resolution regions. The third point is located near marlstone but in the limestone, while the last point is far away from the synthetic marlstone. The distributions are shown in Fig. 10. Similar to the resistivity patterns in Fig. 9, the sample mean of the posterior resistivity distributions from ADVI match perfectly, although they are biased from the true value. However, in Fig. 10(b), the posterior distribution from SVGD exhibits a bimodal pattern, with ‘particles’ clustering in two peaks

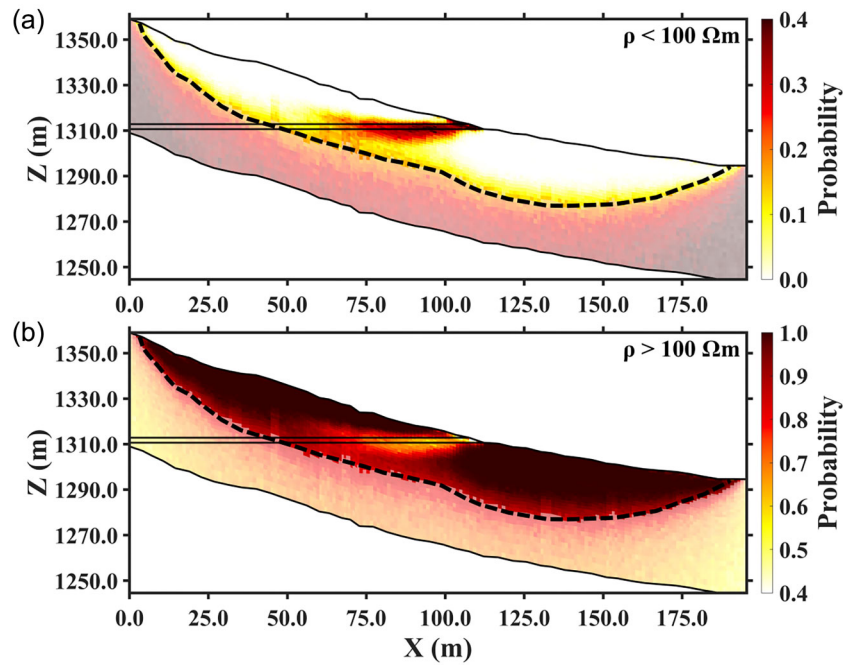


Figure 11. The probability distributions of the model validation. (a) The marlstone probability distributions with a resistivity less than $100 \Omega\text{m}$; (b) the limestone probability distributions with a resistivity more than $100 \Omega\text{m}$. The black solid lines represent the true boundaries between limestone and marlstone. The black dashed lines represent the boundary between the high- and low-resolution regions. The translucent region below the black dotted line represents the low-resolution region, where anomalies are difficult to capture.

that closely match the true resistivities of marlstone and limestone. Although the sample mean from SVGD or ADVI and inverted resistivity from R2 are very close to each other, they clearly deviate from the true resistivity value, which can be misleading in interpretation. This particular distribution highlights the significance of a multimodal posterior distribution in ERT inversion and explains the main reason for the high STD in this region in SVGD. We will revisit this in the Discussion section. For the distributions shown in Figs 10(a) and (c), although the ‘particles’ cluster in a high-resistivity region, there remains a probability (albeit low) of existence resistivity representing the marlstone. For the posterior distribution in the location far away from the marlstone feature (Fig. 10d), the ‘particles’ mainly gather around the high-resistivity value, indicating low probability of marlstone presence.

As demonstrated above, relying on a single estimate (e.g. the sample mean or a representative inverted resistivity) can be misleading and insufficient to capture the full characteristics of ERT results due to the non-uniqueness of the geophysical inversion. The posterior distribution of resistivities can help improve interpretation, although visualizing this for all cells is impossible. One approach to address this is to present the results in terms of a probability of exceeding a specific resistivity threshold, as used by, for example, C.H.M. Tso *et al.* (2021). To illustrate this, we selected a resistivity threshold of $100 \Omega\text{m}$ to represent the marlstone—limestone contrast, as shown in Fig. 11. The results reveal that possible region of the marlstone is much larger than that in the true model, indicating the limited resolution of ERT method itself. For the limestone background, regions far away from the marlstone layer show probabilities approaching 100 per cent, whereas regions in or near the marlstone layer still exhibit probabilities over 40 per cent. It suggests that the multimodal nature of the resistivity distributions is significant: In the known target area, there is a high probability of the background rock type (limestone).

4.3 Probabilistic interpretation of the field data

In this section, we reinterpret inversion of the field results in terms of resistivity probabilities. Here, we still follow the categories in the previous study to represent different structures (Q. Cheng *et al.* 2019): (i) soil layer or marlstone (resistivity $< 100 \Omega\text{m}$); (ii) extensively weathered rock ($100 \Omega\text{m} < \text{resistivity} < 400 \Omega\text{m}$); (iii) compact limestone (resistivity $> 400 \Omega\text{m}$).

The overall probability distributions are shown in Fig. 12. Due to the complex field measurement environment, the depth of the high-resolution region is much shallower than the synthetic field data study. Based on the probability distribution, the subsurface is divided into six different structural regions. The representative resistivity posterior distributions for these regions are illustrated in Fig. 13.

Region I is interpreted as compact limestone because of over 90 per cent probability of a resistivity greater than $1000 \Omega\text{m}$. Region III is located near the wedge-shaped low-resistivity layer previously identified as marlstone (Q. Cheng *et al.* 2019). However, the resistivity distribution in Fig. 13(c) shows that the resistivity here is probably lower than originally interpreted. This further suggests that the applying smooth regularization may be inappropriate when dealing with such significant resistivity contrasts (e.g. $< 100 \Omega\text{m}$ versus $>$

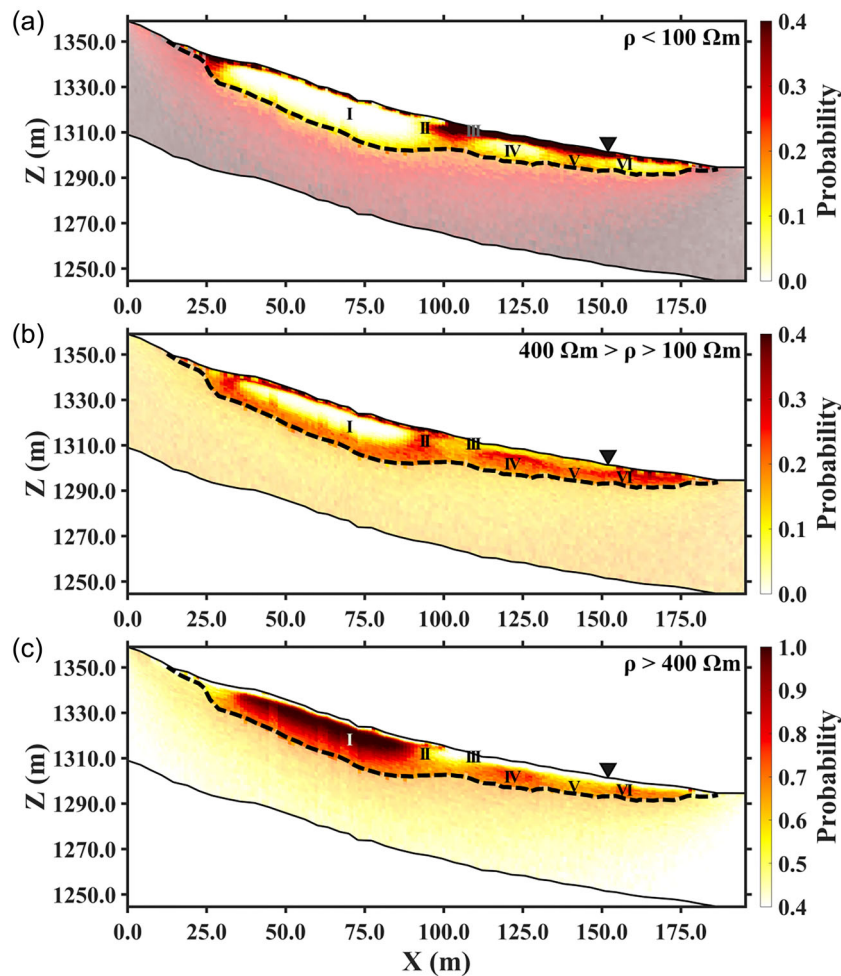


Figure 12. Probability distributions for the Chenqi field data. (a) Probability distribution with a resistivity less than $100 \Omega\text{m}$; (b) probability distribution with a resistivity more than $100 \Omega\text{m}$ but less than $400 \Omega\text{m}$; (c) probability distribution with a resistivity more than $400 \Omega\text{m}$. The black dotted lines represent the boundary between the high- and low-resolution regions. The translucent region below the black dashed line represent the low-resolution region, where anomalies are difficult to capture. The black triangle in each image shows the location of the spring. The posterior distributions for the six locations I–VI are shown in Fig. 13.

$3000 \Omega\text{m}$). The bottom of Region III is connected with the high- and low-resolution boundary, implying that low-resistivity marlstone may extend further downwards along this interface but remains undetected due to the limited resolution of the ERT method.

Region II is located between Regions I and III, which was interpreted as extensive weathering in the previous study (Q. Cheng *et al.* 2019). This interpretation is supported by the resistivity distributions as the ‘particles’ gather between 100 and $400 \Omega\text{m}$. However, as shown in Fig. 13(b), the presence of a high-resistivity ‘tail’ suggests that the possibility of compact limestone in this region cannot be fully excluded. Therefore, additional evidence from other geophysical methods or invasive sampling may be valuable for confirmation.

A spring is located along the ERT survey line, as indicated by the black triangle in each of the images in Fig. 12. It is positioned at the surface above the boundary between Regions V and VI (see Figs 13e and f). Given that these distributions do not indicate a high probability of low resistivity, it would appear that the spring is fed laterally (e.g. from hydraulic impedance at the upper surface of the marlstone layer) rather than from a deeper source.

5 DISCUSSION

In this paper, we applied the SVGD method to quantify resistivity distributions and their associated uncertainties in ERT. Both synthetic and field experiments indicate that SVGD can effectively approximate the posterior pdf, providing some significant advantages over conventional methods and some new insights into uncertainty quantification in ERT, which we discuss in more detail in this section.

The synthetic experiments on configuration and noise effects demonstrate that uncertainty in ERT arises from multiple aspects, each having a significant influence on the final inversion results. It appears that the overall uncertainty is comprehensively determined by a combination of anomaly and measurement effects. In terms of anomaly effects, the trade-off between the shape of a feature and the magnitude of the resistivity leads to a high STD in anomaly regions, as already discussed by E. Galetti *et al.* (2015) and X. Zhang

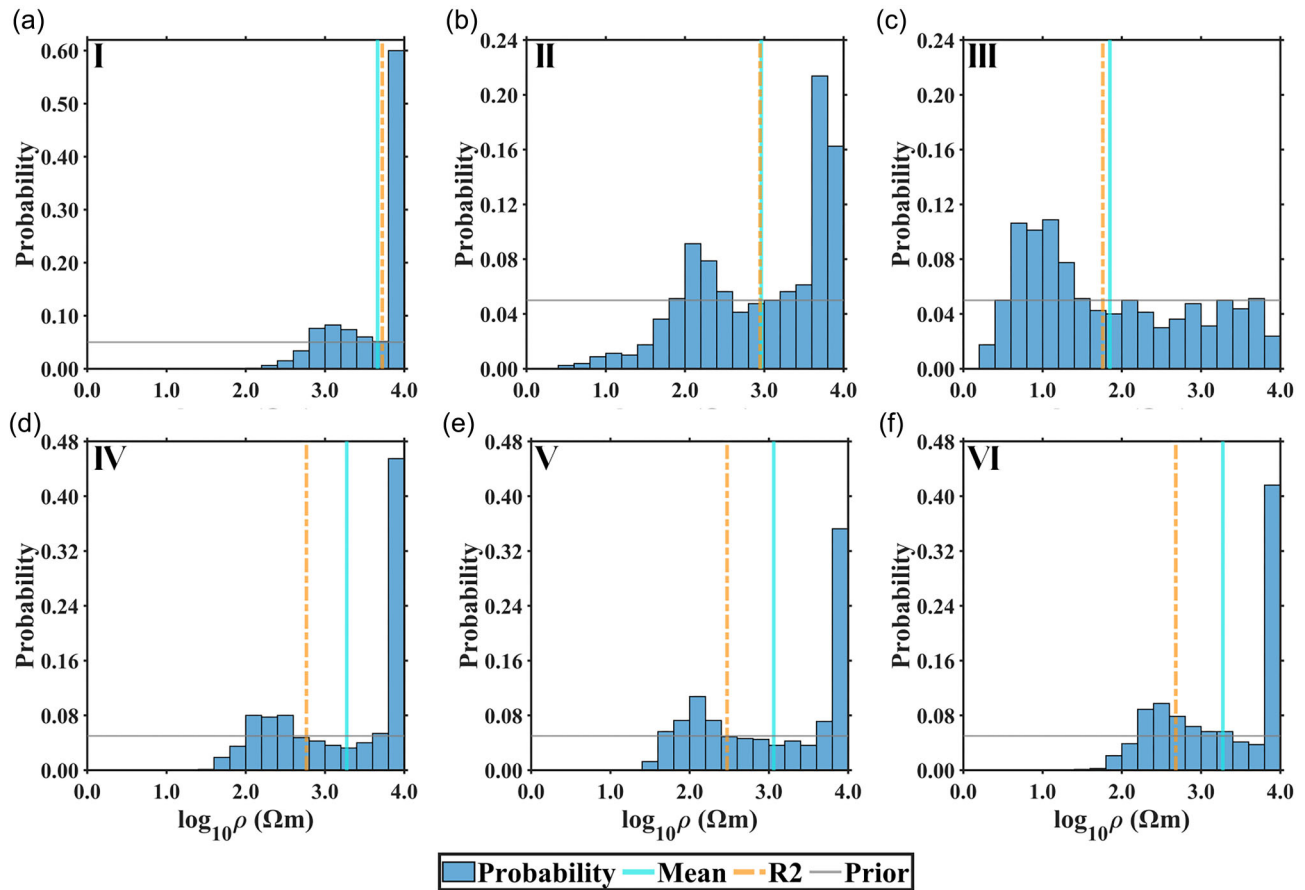


Figure 13. The resistivity distributions of the field data for the Chenqi watershed field data at regions I–VI, respectively. The locations of the six regions are shown in Fig. 12.

et al. (2018). The model validation in Fig. 9 also supports this. It provides an important insight: A high STD does not always indicate high errors. Instead, it may reflect the multimodal nature of the posterior resistivity distributions. Different electrode configurations process different sensitivity distributions (e.g. A. Binley & L. Slater 2020), thus clearly resulting in different resistivity patterns and uncertainties. Regarding effects of measurement noise, there have been very few studies quantifying the associated uncertainties. Our experiments have revealed that noise does not always cause an increase in uncertainty. In regions associated with an anomaly, higher noise levels may reduce resolution, which in turn can reduce the uncertainty arising from anomaly effects. This suggests that uncertainty quantification should not involve only the anomalies and the measurement configurations but also need to treat the noise levels as a key contributor to uncertainty.

SVGD offers a clear advantage in effectively and quantitatively capturing the non-uniqueness of geophysical inversion. Conventional optimization methods typically provide a single deterministic optimal solution, thereby ignoring the existence of the other possible solutions. In this case, model appraisal using qualitative tools like MRM only evaluates the uncertainty associated with the inverted resistivity model itself. Instead, SVGD generates an ensemble of possible geophysical solutions, each consistent with the observed data well. Therefore, these samples can be used to quantify uncertainty from the non-uniqueness of the geophysical inversion (S. Wu *et al.* 2025). In our experiments, we observed that the resistivity distributions are often non-Gaussian and exhibit multimodal probability distributions, as shown in Figs 4 and 10. Such multimodal characteristics were also illustrated in Z.T. Khabaz *et al.* (2024). Due to this feature, the sample mean alone is insufficient as a representation of ERT inversion results (E. Galetti & A. Curtis 2018) and can be misleading or result in incorrect interpretation. There is, therefore, a need to focus on posterior resistivity distributions. A simple approach is to divide the distribution into different intervals to represent different media to explore the probability, although the threshold may seem to be somewhat subjective.

Another apparent advantage of the SVGD approach is its ability to avoid the use of spatial regularization. Such an advantage can also be seen in seismic VI (H. Yang *et al.* 2025). Regularization is essential in conventional geophysical optimization and has been extensively developed to support various geological structures (C.G. Farquharson 2008; F. Nguyen *et al.* 2016; Y. Shi *et al.* 2020; K. Ishizu *et al.* 2025) and hydrologic property distributions (T.-C.J. Yeh *et al.* 2002; N. Linde *et al.* 2006). Nonetheless, regularization appears to be viewed by some unfavourably in hydrogeophysics (N. Linde *et al.* 2017). Fundamentally, regularization imposes assumptions on the subsurface structure, which can be treated as a form of prior information (X.B. Zhao & A. Curtis 2024b). Such prior information often

excludes the possibility of shape effects and only considers resistivity distributions. This helps to stabilize deterministic inversions, but an inappropriate regularization approach may trigger artifacts due to the limited resolution (A.M. Carey *et al.* 2017). This constraint presents a significant challenge in hydrogeophysical applications where inverted resistivity values are often transformed into hydrogeological parameter (e.g. fluid saturation, porosity, etc.) based on petrophysical relationships to parametrize hydrogeological models (J. Beaujean *et al.* 2014; A. Revil *et al.* 2020). However, as indicated in the results of our synthetic experiments, regularization causes shifts in resistivity values given the prior structure. In this case, the shift will also be transmitted to errors in estimated hydrogeological parameters, which warrants attention in the interpretation. Moreover, our results show that the sample mean from SVGD also exhibit artifacts due to overfitting the data using elements with fixed size, which was also observed in seismic VI (X. Zhang & A. Curtis 2020). The use of more flexible elements, such as Voronoi cells, may help to address this issue (E. Galetti & A. Curtis 2018; X. Zhang & A. Curtis 2020). Alternatively, the level set parameterisation in C.H.M. Tso *et al.* (2021, 2024) is also another approach to tackle this problem. Both inversion approaches are applicable across different probabilistic inversion frameworks (EKI, MCMC, SVGD etc.). In practice, given the high-computational efficiency of the conventional approach, it is recommended interpreting the sample mean from SVGD with the inverted image to aid explanation.

Some methods for uncertainty quantification, such as EKI (C.H.M. Tso *et al.* 2021, 2024), certain deep learning inversion methods (F. Rincón *et al.* 2025) and another VI method ADVI (A. Kucukelbir *et al.* 2017), rely on the assumption that posterior distributions follow a Gaussian distribution, resulting that the computed uncertainties tend to be more biased (X. Zhang & A. Curtis 2020), especially when the distribution is non-Gaussian. Nevertheless, given its high-computational efficiency of ADVI, some enhanced VI methods, such as boosting variational inference (X.B. Zhao & A. Curtis 2024a), may be a more promising approach. Comparing SVGD with EKI, both methods involve forward modelling, but the Jacobian-free feature of EKI approach may have an advantage in terms of computational requirements compared to SVGD, particularly for multiphysics problems (e.g. coupled hydrogeophysics inversion using a flow simulator). For simpler problems, for example, ERT, SVGD shows great potential to be used in quantifying distributions and uncertainties of the hydrogeological parameters directly. Although SVGD requires the Jacobian of the forward model, this gradient can be easily converted to that with respect to hydrogeological parameters (e.g. fluid saturation or porosity) through defined petrophysical relationships (e.g. F.M. Wagner *et al.* 2019). Note that this is without considering the inherent nonlinearity and uncertainties in petrophysical relationships (N. Linde *et al.* 2017; C. Brunetti & N. Linde 2018). Combined with multimodal resistivity distributions in ERT, the distributions of hydrogeological parameters can also be multimodal (an example is indicated in J.P. Boyd *et al.* (2024b)), which may lead to posterior distributions that are highly complex and difficult to interpret, making hydrogeophysical inversion challenging. This suggests that geophysical measurements should not be used in isolation. More evidence from other geophysical or other methods should be provided to reduce the uncertainty from ERT results. However, when lacking the external information (i.e. borehole or hydrogeology data) to validate the subsurface structure, the probabilistic interpretation using the SVGD method is a more reliable approach to avoid potential misleading. Furthermore, given the multimodal resistivity distributions, filters with multimodal imaging capabilities (e.g. S.G. Penny & T. Miyoshi 2016), may offer certain advantages and worthy of further exploration.

Future work should focus on improving computational efficiency, which remains a common challenge in probabilistic inversion framework. Although a direct comparison between SVGD and MCMC methods was not conducted in this paper, we believe that SVGD is computationally more practical than MCMC methods. This is because compared to random samplings in MCMC methods, SVGD method uses few samples to update the posterior distributions based on optimization using the Jacobian matrix, which is definitely of great efficiency, as proved in many studies in geophysics (X. Zhang & A. Curtis 2020; X.B. Zhao & A. Curtis 2024a). Fortunately, the numerical simulations of ‘particles’ are mutually independent, which means that this process can be carried out completely parallel (X. Zhang & A. Curtis 2021). Therefore, a large number of threads may help to improve the computational efficiency. Some deep learning methods for rapid numerical simulations, such as non-intrusive reduced basis (N. Lindner *et al.* 2025; A. Quiaro *et al.* 2025), exhibit great potential to accelerate the massive forward modelling tasks with limited loss of accuracy. This advantage may be fully exploited in 3-D simulations as well as in time-lapse resistivity monitoring (in 2-D or even 3-D), particularly for long-term monitoring with fixed configurations.

6 CONCLUSIONS

We have applied the SVGD approach to quantify resistivity distributions and uncertainties in ERT, and compared its performance with conventional inversion methods based on both synthetic and field experiments. Compared to conventional inversion methods, SVGD offers more quantitative information about subsurface structures, including detection scales, occurrence of high-resolution regions and multimodal posterior resistivity probabilities. Moreover, it also avoids the biases introduced by regularization or the Gaussian prior. Compared to MCMC method, SVGD is attractive for uncertainty estimation due to its requirement for fewer samples, leading to greater computational efficiency. Based on our findings, we recommend performing probabilistic interpretation and recognizing resistivity distributions within ERT results to fully demonstrate the uncertainty distributions of ERT-derived models of the subsurface.

In addition, a thorough understanding of uncertainty sources is also critical, as uncertainty in ERT is simultaneously determined by various factors such as anomalies and measurements. Therefore, uncertainty quantification should be considered combined with

noise levels to evaluate the relative weighting between the anomaly and noise effects. Furthermore, given the multimodal resistivity distributions in ERT, hydrogeophysical inversion methods specifically based on unimodal assumptions (ensemble Kalman filter, EnKF, for example), should also adequately consider the potential multimodal nature of the hydrological parameters, which should be comprehensively investigated in the future.

Finally, we recognize that not all applications of geophysics to hydrological problems warrant uncertainty estimation. The need will depend on the consequences of incorrect interpretation or translation to hydrological parameters.

ACKNOWLEDGMENTS

The research was supported by National Key Research and Development Program of China (No. 2022YFC3003402), National Natural Science Foundation of China (No. NSFC42474192) and China Scholarship Council (No. CSC202406170185). We would like to thank Prof. Andrew Curtis and Dr Xuebin Zhao from The University of Edinburgh for their valuable assistance. The authors also would like to thank the researchers who participated in the field work but were not listed as co-authors. We also sincerely appreciate three anonymous reviewers for their constructive and insightful comments. The field data originated from a project supported by the UK Natural Environment Research Council (NERC) Grant NE/N007409/1 awarded to Lancaster University.

SUPPORTING INFORMATION

Supplementary data are available at [GJI](#) online.

Figure S1. The sample mean and STD obtained from SVGD using different numbers of ‘particles’. a)-b) 400 ‘particles’; c)-d) 800 ‘particles’; e)-f) 1200 ‘particles’.

Figure S2. The sample mean and STD obtained from SVGD using kernels. a)-b) gradient kernel; c)-d) RBF kernel; e)-f) variance kernel.

Table S1. The iteration numbers and computational time for different ‘particle’ numbers.

Table S2. The iteration numbers and final RMS for different kernels.

Please note: Oxford University Press are not responsible for the content or functionality of any supporting materials supplied by the authors. Any queries (other than missing material) should be directed to the corresponding author for the article.

DATA AVAILABILITY

The code is modified from open-source Variational Inversion Package (VIP; X. Zhang & A. Curtis 2024a). The modified ERTVI code and data in this paper is available in J. Yan & A. Binley (2025). The ERT simulation code is a modified version of R2, which provides forward data and Jacobian as a binary file to improve computational efficiency. The standard version of R2 (which also has an option to generate a Jacobian matrix) can be downloaded at A. Binley (2023).

REFERENCES

- Aleardi, M., Vinciguerra, A. & Hojat, A., 2021. A geostatistical Markov chain Monte Carlo inversion algorithm for electrical resistivity tomography, *Near Surf. Geophys.*, **19**(1), 7–26.
- Alemie, W. & Sacchi, M.D., 2011. High-resolution three-term AVO inversion by means of a Trivariate Cauchy probability distribution, *Geophysics*, **76**(3), R43–R55.
- Alumbaugh, D.L. & Newman, G.A., 2000. Image appraisal for 2-D and 3-D electromagnetic inversion, *Geophysics*, **65**(5), 1455–1467.
- Aster, R.C., Borchers, B. & Thurber, C.H. 2018. *Parameter Estimation and Inverse Problems*, Elsevier.
- Beaujean, J., Nguyen, F., Kemna, A., Antonsson, A. & Engesgaard, P., 2014. Calibration of seawater intrusion models: inverse parameter estimation using surface electrical resistivity tomography and borehole data, *Water Resour. Res.*, **50**(8), 6828–6849.
- Beven, K. & Binley, A., 2014. GLUE: 20 years on, *Hydrol. Process.*, **28**(24), 5897–5918.
- Binley, A., 2023. R2 (v4.11), <http://www.es.lancs.ac.uk/people/amb/Freeware/R2/R2.htm> (accessed 1 September 2025)
- Binley, A., Cassiani, G., Middleton, R. & Winship, P., 2002. Vadose zone flow model parameterisation using cross-borehole radar and resistivity imaging, *J. Hydrol.*, **267**(3–4), 147–159.
- Binley, A., Hubbard, S.S., Huisman, J.A., Revil, A., Robinson, D.A., Singha, K. & Slater, L.D., 2015. The emergence of hydrogeophysics for improved understanding of subsurface processes over multiple scales, *Water Resour. Res.*, **51**(6), 3837–3866.
- Binley, A. & Slater, L., 2020. *Resistivity and Induced Polarization: Theory and Applications to the Near-Surface Earth*, Cambridge Univ. Press.
- Blei, D.M., Kucukelbir, A. & McAuliffe, J.D., 2017. Variational inference: a review for statisticians, *J. Am. Stat. Assoc.*, **112**(518), 859–877.
- Boyd, J.P., Binley, A., Wilkinson, P., Holmes, J., Bruce, E. & Chambers, J., 2024a. Practical considerations for using petrophysics and geoelectrical methods on clay rich landslides, *Eng. Geol.*, **334**, 107 506.
- Boyd, J.P., Chambers, J.E., Wilkinson, P.B., Meldrum, P.I., Bruce, E. & Binley, A., 2024b. Coupled hydrogeophysical modeling to constrain unsaturated soil parameters for a slow-moving landslide, *Water Resour. Res.*, **60**(10), e2023WR036319.
- Brunetti, C. & Linde, N., 2018. Impact of petrophysical uncertainty on Bayesian hydrogeophysical inversion and model selection, *Adv. Water Resour.*, **111**, 346–359.

- Camporese, M., Cassiani, G., Deiana, R., Salandin, P. & Binley, A., 2015. Coupled and uncoupled hydrogeophysical inversions using ensemble Kalman filter assimilation of ERT-monitored tracer test data, *Water Resour. Res.*, **51**(5), 3277–3291.
- Carey, A.M., Paige, G.B., Carr, B.J. & Dogan, M., 2017. Forward modeling to investigate inversion artifacts resulting from time-lapse electrical resistivity tomography during rainfall simulations, *J. Appl. Geophys.*, **145**, 39–49.
- Cassiani, G., Godio, A., Stocco, S., Villa, A., Deiana, R., Frattini, P. & Rossi, M., 2009. Monitoring the hydrologic behaviour of a mountain slope via time-lapse electrical resistivity tomography, *Near Surf. Geophys.*, **7**(5-6), 475–486.
- Chang, J.C., Savage, V.M. & Chou, T., 2014. A path-integral approach to Bayesian inference for inverse problems using the semiclassical approximation, *J. Stat. Phys.*, **157**, 582–602.
- Chen, H. et al. 2025. Development of an ERT-based framework for Bentonite buffers monitoring from laboratory tests: 2. Quantitative moisture dynamics estimation model, *J. Geophys. Res.: Solid Earth*, **130**(8), e2024JB030799.
- Chen, X., Zhang, Z., Soulsby, C., Cheng, Q., Binley, A., Jiang, R. & Tao, M., 2018. Characterizing the heterogeneity of karst critical zone and its hydrological function: an integrated approach, *Hydrol. Process.*, **32**(19), 2932–2946.
- Cheng, Q., Chen, X., Tao, M. & Binley, A., 2019. Characterization of karst structures using quasi-3D electrical resistivity tomography, *Environ. Earth Sci.*, **78**(9), 285.
- Ciraula, D.A., Carr, B.J. & Sims, K.W.W., 2023. Geophysical imaging of the shallow geyser and hydrothermal reservoir structures of Spouter Geyser, Yellowstone National Park: geyser Dynamics I, *J. Geophys. Res.: Solid Earth*, **128**(2).
- Claes, N., Paige, G.B., Grana, D. & Parsekian, A.D., 2020. Parameterization of a hydrologic model with geophysical data to simulate observed subsurface return flow paths, *Vadose Zone J.*, **19**(1).
- Codd, A.L. & Gross, L., 2018. Electrical Resistivity Tomography using a finite element based BFGS algorithm with algebraic multigrid preconditioning, *Geophys. J. Int.*, **212**(3), 2073–2087.
- Curtis, A. & Lomax, A., 2001. Prior information, sampling distributions, and the curse of dimensionality, *Geophysics*, **66**(2), 372–378.
- Dahlin, T. & Zhou, B., 2004. A numerical comparison of 2D resistivity imaging with 10 electrode arrays, *Geophys. Prospect.*, **52**(5), 379–398.
- Demoment, G. & Idier, J., 2008. Main approaches to the regularization of ill-posed problems, In *Bayesian Approach to Inverse Problems*, pp. 41–58, ISTE, London; Wiley, Hoboken, NJ.
- Duchi, J., Hazan, E. & Singer, Y., 2011. Adaptive subgradient methods for online learning and stochastic optimization, *J. Mach. Learn. Res.*, **12**, 2121–2159.
- Farquharson, C.G., 2008. Constructing piecewise-constant models in multidimensional minimum-structure inversions, *Geophysics*, **73**(1), K1–K9.
- Galetti, E. & Curtis, A., 2018. Transdimensional electrical resistivity tomography, *J. Geophys. Res.: Solid Earth*, **123**(8), 6347–6377.
- Galetti, E., Curtis, A., Meles, G.A. & Baptie, B., 2015. Uncertainty loops in travel-time tomography from nonlinear wave physics, *Phys. Rev. Lett.*, **114**(14).
- Gallagher, K., Charvin, K., Nielsen, S., Sambridge, M. & Stephenson, J., 2009. Markov chain Monte Carlo (MCMC) sampling methods to determine optimal models, model resolution and model choice for Earth Science problems, *Mar. Petrol. Geol.*, **26**(4), 525–535.
- Ganguly, A. & Earp, S.W., 2021. An introduction to variational inference, arXiv preprint arXiv:2108.13083.
- Günther, T., Rücker, C. & Spitzer, K., 2006. Three-dimensional modelling and inversion of dc resistivity data incorporating topography — II. Inversion, *Geophys. J. Int.*, **166**(2), 506–517.
- Hubbard, S.S. & Rubin, Y., 2000. Hydrogeological parameter estimation using geophysical data: a review of selected techniques, *J. Contam. Hydrol.*, **45**(1–2), 3–34.
- Irving, J. & Singha, K., 2010. Stochastic inversion of tracer test and electrical geophysical data to estimate hydraulic conductivities, *Water Resour. Res.*, **46**.
- Ishizu, K., Goto, T.-N., Fukahata, Y., Koike, K., Vachirathienchai, C. & Siripunvaraporn, W., 2025. Inversion algorithm determining sharp boundaries in electrical resistivity tomography, *Geophysics*, **90**(3), WA221–WA233.
- Johnson, T.C. et al. 2021. 4D proxy imaging of fracture dilation and stress shadowing using electrical resistivity tomography during high pressure injections into a dense rock formation, *J. Geophys. Res.: Solid Earth*, **126**(11).
- Kang, X.Y., Kokkinaki, A., Kitanidis, P.K., Shi, X.Q., Lee, J., Mo, S.X. & Wu, J.C., 2021. Hydrogeophysical Characterization of Nonstationary DNAPL Source Zones by Integrating a Convolutional Variational Autoencoder and Ensemble Smoother, *Water Resour. Res.*, **57**(2).
- Kemna, A., 2000. *Tomographic Inversion of Complex Resistivity: Theory and Application*, PhD thesis, Der Andere Verlag.
- Kemna, A., Vanderborght, J., Kulesa, B. & Vereecken, H., 2002. Imaging and characterisation of subsurface solute transport using electrical resistivity tomography (ERT) and equivalent transport models, *J. Hydrol.*, **267**(3–4), 125–146.
- Khabaz, Z.T., Ghanati, R. & Bérubé, C.L., 2024. Uncertainty quantification in electrical resistivity tomography inversion: hybridizing block-wise bootstrapping with geostatistics, *Geophys. J. Int.*, **239**(3), 1576–1596.
- Kucukelbir, A., Tran, D., Ranganath, R., Gelman, A. & Blei, D.M., 2017. Automatic differentiation variational inference, *J. Mach. Learn. Res.*, **18**, 1–45.
- Kullback, S. & Leibler, R.A., 1951. On Information and Sufficiency, *Ann. Math. Statist.*, **22**(1), 79–86.
- LaBrecque, D.J., Miletto, M., Daily, W., Ramirez, A. & Owen, E., 1996. The effects of noise on Occam's inversion of resistivity tomography data, *Geophysics*, **61**(2), 538–548.
- Lan, X.X., Zou, C.C., Peng, C. & Wu, C.W., 2023. Uncertainty quantification in intelligent-based electrical resistivity tomography image reconstruction with Monte Carlo dropout strategy, *IEEE Trans. Geosci. Remote Sens.*, **61**, 1–16.
- Li, A., Parsekian, A.D., Grana, D. & Carr, B.J., 2025. Quantification of measurement uncertainty in electrical resistivity tomography data and its effect on the inverted resistivity model, *Geophysics*, **90**(3), WA275–WA291.
- Linde, N., Finsterle, S. & Hubbard, S., 2006. Inversion of tracer test data using tomographic constraints, *Water Resour. Res.*, **42**(4).
- Linde, N., Ginsbourger, D., Irving, J., Nobile, F. & Doucet, A., 2017. On uncertainty quantification in hydrogeology and hydrogeophysics, *Adv. Water Resour.*, **110**, 166–181.
- Lindner, N., Degen, D., Grayver, A. & Wellmann, F., 2025. Sensitivity analysis using physics-based machine learning: an example from surrogate modelling for magnetotellurics, *Geophys. J. Int.*, **242**(1).
- Liu, B., Li, S.C., Li, S.C., Nie, L.C., Zhong, S.H., Li, L.P., Song, J. & Liu, Z.Y., 2012. 3D electrical resistivity inversion with least-squares method based on inequality constraint and its computation efficiency optimization, *Chin. J. Geophys.-Ch.*, **55**(1), 260–268.
- Liu, B., Pang, Y., Jiang, P., Liu, Z., Liu, B., Zhang, Y., Cai, Y. & Liu, J., 2023. Physics-driven deep learning inversion for direct current resistivity survey data, *IEEE Trans. Geosci. Remote Sens.*, **61**, 1–11.
- Liu, Q., 2017. Stein variational gradient descent as gradient flow, *Adv. Neural Inf. Process. Syst.*, **30**(Nips 2017), 3115–3123.
- Liu, Q., Lee, J.D. & Jordan, M., 2016. A kernelized stein discrepancy for Goodness-of-fit tests, *International Conference on Machine Learning*, **Vol. 48**, pp. 276–284, PMLR.

- Liu, Q. & Wang, D.L., 2016. Stein variational gradient descent: a general purpose Bayesian inference algorithm, *Adv. Neural Inf. Process. Syst.*, **29**(Nips 2016), 2378–2386.
- Lubczynski, M.W., Leblanc, M. & Batelaan, O., 2024. Remote sensing and hydrogeophysics give a new impetus to integrated hydrological models: a review, *J. Hydrol.*, **633**.
- Menke, W., 2015. Review of the generalized least squares method, *Surv. Geophys.*, **36**(1), 1–25.
- Miltenberger, A., Uhlemann, S., Mukerji, T., Williams, K., Dafflon, B., Wang, L. & Wainwright, H., 2021. Probabilistic evaluation of geoscientific hypotheses with geophysical data: application to electrical resistivity imaging of a fractured bedrock zone, *J. Geophys. Res.: Solid Earth*, **126**(9), e2021JB021767.
- Mosegaard, K. & Tarantola, A., 1995. Monte-Carlo sampling of solutions to inverse problems, *J. Geophys. Res.: Solid Earth*, **100**(B7), 12 431–12 447.
- Nguyen, F., Kemna, A., Robert, T. & Hermans, T., 2016. Data-driven selection of the minimum-gradient support parameter in time-lapse focused electric imaging, *Geophysics*, **81**(1), A1–A5.
- Oldenburger, G.A., Routh, P.S. & Knoll, M.D., 2007. Model reliability for 3D electrical resistivity tomography: application of the volume of investigation index to a time-lapse monitoring experiment, *Geophysics*, **72**(4), F167–F175.
- Oldenburg, D.W. & Li, Y.G., 1999. Estimating depth of investigation in dc resistivity and IP surveys, *Geophysics*, **64**(2), 403–416.
- Oware, E.K., Irving, J. & Hermans, T., 2019. Basis-constrained Bayesian Markov-chain Monte Carlo difference inversion for geoelectrical monitoring of hydrogeologic processes, *Geophysics*, **84**(4), A37–A42.
- Penny, S.G. & Miyoshi, T., 2016. A local particle filter for high-dimensional geophysical systems, *Nonlin. Processes Geophys.*, **23**(6), 391–405.
- Pidlisecky, A., Haber, E. & Knight, R., 2007. RESINVM3D: a 3D resistivity inversion package, *Geophysics*, **72**(2), H1–H10.
- Pleasants, M.S., Neves, F.D., Parsekian, A.D., Befus, K.M. & Kelleners, T.J., 2022. Hydrogeophysical inversion of time-lapse ERT data to determine hillslope subsurface hydraulic properties, *Water Resour. Res.*, **58**(4). doi: 10.1029/2021WR031073.
- Pollock, D. & Cirpka, O.A., 2012. Fully coupled hydrogeophysical inversion of a laboratory salt tracer experiment monitored by electrical resistivity tomography, *Water Resour. Res.*, **48**.
- Quiaro, A., Liu, D. & Sacchi, M.D., 2025. Nonintrusive reduced basis approximation to the solution of the Helmholtz equation: the magnetotellurics case, *Geophysics*, **90**(3), WA323–WA337.
- Ramirez, A.L. et al., 2005. Stochastic inversion of electrical resistivity changes using a Markov Chain Monte Carlo approach, *J. Geophys. Res.: Solid Earth*, **110**(B2).
- Rasmussen, C.E. & Williams, C.K.I., 2005. *Gaussian Processes for Machine Learning*, The MIT Press.
- Revil, A., Soueid Ahmed, A., Coperey, A., Ravanel, L., Sharma, R. & Panwar, N., 2020. Induced polarization as a tool to characterize shallow landslides, *J. Hydrol.*, **589**, 125–136.
- Rincón, F., Aleardi, M., Tognarelli, A. & Stucchi, E., 2025. Physics-guided deep-learning direct current-resistivity inversion with uncertainty quantification, *Geophysics*, **90**(5), E165–E179.
- Shi, Y., Rao, Z., Wang, C., Fan, Y., Zhang, X. & Wang, M., 2020. Total variation regularization based on iteratively reweighted least-squares method for electrical resistance tomography, *IEEE Trans. Instrum. Meas.*, **69**(6), 3576–3586.
- Shlens, J., 2014. Notes on kullback-leibler divergence and likelihood, arXiv preprint arXiv:1404.2000.
- Tarantola, A., 1987. *Inverse Problem Theory: Methods for Data Fitting and Model Parameter Estimation*. Elsevier Science.
- Thomas, A., Fortin, J., Vittecoq, B., Aochi, H., Violette, S., Maury, J., Lacquement, F. & Bitri, A., 2024. Hydro-mechanical characterization of a fractured aquifer using groundwater level tidal analysis: effect of pore pressure and seismic dynamic shear stresses on permeability variations, *J. Geophys. Res.: Solid Earth*, **129**(8), e2024JB028847.
- Tran, M.N., Nguyen, T.N. & Dao, V.H., 2021. A practical tutorial on variational Bayes, arXiv preprint arXiv:2103.01327.
- Tso, C.H.M. et al. 2017. Improved characterisation and modelling of measurement errors in electrical resistivity tomography (ERT) surveys, *J. Appl. Geophys.*, **146**, 103–119.
- Tso, C.H.M., Iglesias, M. & Binley, A., 2024. Ensemble Kalman inversion of induced polarization data, *Geophys. J. Int.*, **236**(3), 1877–1900.
- Tso, C.H.M., Iglesias, M., Wilkinson, P., Kuras, O., Chambers, J. & Binley, A., 2021. Efficient multiscale imaging of subsurface resistivity with uncertainty quantification using ensemble Kalman inversion, *Geophys. J. Int.*, **225**(2), 887–905.
- Tso, C.H.M., Kuras, O. & Binley, A., 2019. On the Field Estimation of Moisture Content Using Electrical Geophysics: the Impact of Petrophysical Model Uncertainty, *Water Resour. Res.*, **55**(8), 7196–7211.
- Uhlemann, S. et al. 2017. Four-dimensional imaging of moisture dynamics during landslide reactivation, *J. Geophys. Res.: Earth Surface*, **122**(1), 398–418.
- Van Camp, M., Vanclooster, M., Crommen, O., Petermans, T., Verbeeck, K., Meurers, B., van Dam, T. & Dassargues, A., 2006. Hydrogeological investigations at the Membach station, Belgium, and application to correct long periodic gravity variations, *J. Geophys. Res.: Solid Earth*, **111**(B10).
- Wagner, F.M., Mollaret, C., Günther, T., Kemna, A. & Hauck, C., 2019. Quantitative imaging of water, ice and air in permafrost systems through petrophysical joint inversion of seismic refraction and electrical resistivity data, *Geophys. J. Int.*, **219**(3), 1866–1875.
- Weill, S., Mouche, E. & Patin, J., 2009. A generalized Richards equation for surface/subsurface flow modelling, *J. Hydrol.*, **366**(1–4), 9–20.
- Wu, S., Sun, J. & Chen, J., 2025. Variational inference for geophysical Bayesian inverse problems using normalizing flows: an unsupervised approach to electromagnetic data inversion, *Geophys. J. Int.*, **242**(3).
- Yan, J. & Binley, A., 2025. ERTVI—An Open-source Variational Inference Code for Electrical Resistivity Tomography (v1.0), Zenodo
- Yang, H., Zhang, X. & Zhang, H., 2025. 3-D variational inference-based double-difference seismic tomography method and application to the SAFOD site, California, *Geophys. J. Int.*, **241**(1), 378–404.
- Yeh, T.-C.J., Liu, S., Glass, R.J., Baker, K., Brainard, J.R., Alumbaugh, D. & LaBrecque, D., 2002. A geostatistically based inverse model for electrical resistivity surveys and its applications to vadose zone hydrology, *Water Resour. Res.*, **38**(12), 14–11-14-13.
- Zhang, J.Y., Zhang, R.Y., Carin, L. & Chen, C.Y., 2020. Stochastic particle-optimization sampling and the non-asymptotic convergence theory, *International Conference on Artificial Intelligence and Statistics, Vol 108*, pp. 1877–1886, PMLR.
- Zhang, X. & Curtis, A., 2020. Seismic Tomography Using Variational Inference Methods, *J. Geophys. Res.: Solid Earth*, **125**(4).
- Zhang, X. & Curtis, A., 2021. Bayesian full-waveform inversion with realistic priors, *Geophysics*, **86**(5), A45–A49.
- Zhang, X. & Curtis, A., 2024a. VIP—Variational Inversion Package with example implementations of Bayesian tomographic imaging, *Seismica*, **3**(1).
- Zhang, X. & Curtis, A., 2024b. Bayesian variational time-lapse full waveform inversion, *Geophys. J. Int.*, **237**(3), 1624–1638.
- Zhang, X., Curtis, A., Galetti, E. & de Ridder, S., 2018. 3-D Monte Carlo surface wave tomography, *Geophys. J. Int.*, **215**(3), 1644–1658.
- Zhang, X., Lomas, A., Zhou, M.H., Zheng, Y.R. & Curtis, A., 2023. 3-D Bayesian variational full waveform inversion, *Geophys. J. Int.*, **234**(1), 546–561.

Zhang, X., Nawaz, M.A., Zhao, X.B. & Curtis, A., 2021. An introduction to variational inference in geophysical inverse problems, *Inversion of Geophysical Data*, Vol. 62, pp. 73–140, Elsevier.

Zhao, X.B. & Curtis, A., 2024a. Bayesian inversion, uncertainty analysis and interrogation using boosting variational inference, *J. Geophys. Res.: Solid Earth*, 129(1).

Zhao, X.B. & Curtis, A., 2024b. Physically structured variational inference for Bayesian full waveform inversion, *J. Geophys. Res.: Solid Earth*, 129(11).

APPENDIX A: DERIVATIONS OF THE SVGD APPROACH

Following Q. Liu & D.L. Wang (2016), $q_T(\mathbf{m})$ is defined to represent the transformed probability distribution $q(\mathbf{m})$, given by

$$q_T(\mathbf{m}) = q(\mathbf{T}^{-1}(\mathbf{m})) \cdot |\det(\nabla_{\mathbf{m}}\mathbf{T}(\mathbf{m}))|^{-1}, \quad (\text{A1})$$

where \mathbf{T}^{-1} denotes the inverse map of \mathbf{T} , \det denotes the determinant of the matrix, and $\nabla_{\mathbf{m}}\mathbf{T}(\mathbf{m})$ is the Jacobian matrix of \mathbf{T} with respect to \mathbf{m} . When $|\varepsilon|$ is sufficiently small, the Jacobian $\nabla_{\mathbf{m}}\mathbf{T}(\mathbf{m})$ is full rank and hence \mathbf{T} is invertible.

Based on the basic principles of VI, the KL-divergence between $q_T(\mathbf{m})$ and $p(\mathbf{m}|\mathbf{d}_{\text{obs}})$ is defined and minimized to make the transformed distribution $q_T(\mathbf{m})$ approximate the posterior pdf $p(\mathbf{m}|\mathbf{d}_{\text{obs}})$. To obtain the descent direction of the KL-divergence, its gradient with respect to ε , denoted as $\nabla_{\varepsilon}\text{KL}$, is expressed as (Q. Liu & D.L. Wang 2016)

$$\nabla_{\varepsilon}\text{KL}[q_T(\mathbf{m})||p(\mathbf{m}|\mathbf{d}_{\text{obs}})]|_{\varepsilon=0} = -E_{q(\mathbf{m})}[\text{trace}(\mathbf{A}_{p(\mathbf{m}|\mathbf{d}_{\text{obs}})}\Phi(\mathbf{m}))], \quad (\text{A2})$$

where trace denotes the trace of a matrix. $\mathbf{A}_{p(\mathbf{m}|\mathbf{d}_{\text{obs}})}$ is the Stein operator and defined as:

$$\mathbf{A}_{p(\mathbf{m}|\mathbf{d}_{\text{obs}})}\Phi(\mathbf{m}) = \nabla_{\mathbf{m}}\log p(\mathbf{m}|\mathbf{d}_{\text{obs}})\Phi(\mathbf{m})^{\top} + \nabla_{\mathbf{m}}\Phi(\mathbf{m}). \quad (\text{A3})$$

In eq. (A-2), the problem of minimizing the KL-divergence is naturally converted to maximizing the expectation $E_{q(\mathbf{m})}[\text{trace}(\mathbf{A}_{p(\mathbf{m}|\mathbf{d}_{\text{obs}})}\Phi(\mathbf{m}))]$, which is also the steepest descent direction. The problem then constitutes a reproducing kernel Hilbert space (RKHS) optimization problem for the Kernelized Stein Discrepancy $S(q(\mathbf{m}), p(\mathbf{m}|\mathbf{d}_{\text{obs}}))$, written as (Q. Liu & D.L. Wang 2016)

$$S(q(\mathbf{m}), p(\mathbf{m}|\mathbf{d}_{\text{obs}})) = \underset{\phi \in H^d, \|\phi\|_{H^d} \leq 1}{\text{argmax}} E_{q(\mathbf{m})}[\text{trace}(\mathbf{A}_{p(\mathbf{m}|\mathbf{d}_{\text{obs}})}\phi(\mathbf{m}))]^2, \quad (\text{A4})$$

where H^d denotes RKHS. According to Q. Liu *et al.* (2016), the solution to this optimal problem is

$$\Phi^*(\mathbf{m}) = E_{q(\mathbf{m})}[\mathbf{A}_{p(\mathbf{m}|\mathbf{d}_{\text{obs}})}k(\mathbf{m}', \mathbf{m})], \quad (\text{A5})$$

where $\Phi^*(\mathbf{m})$ is the optimal direction from a set of initial distributions $\{\mathbf{m}_i^0\}$. $k(\mathbf{m}', \mathbf{m})$ is a positive definite kernel. The optimal direction $\Phi^*(\mathbf{m})$ can be expressed as:

$$\Phi_i^*(\mathbf{m}_i^l) = \frac{1}{n} \sum_{j=1}^n \left[k(\mathbf{m}_j^l, \mathbf{m}_i^l) \nabla_{\mathbf{m}_j^l} \log p(\mathbf{m}_j^l|\mathbf{d}_{\text{obs}}) + \nabla_{\mathbf{m}_j^l} k(\mathbf{m}_j^l, \mathbf{m}_i^l) \right]. \quad (\text{A6})$$